UNIVERSITY OF CALIFORNIA,
IRVINE

The Effect of Manufacturing Defects on Compressive Strength of Polymeric Lattices Fabricated via Fused Deposition Modeling

THESIS

submitted in partial satisfaction of the requirements
for the degree of

MASTER OF SCIENCE

in Mechanical and Aerospace Engineering

by

Bianca Lis Rossi Dias Endo

Thesis Committee:
Associate Professor Lorenzo Valdevit, Chair
Associate Professor Timothy J. Rupert
Professor J. Michael McCarthy

2017

DEDICATION

To my parents and friends

Thank you for your love,
support and encouragement.

TABLE OF CONTENTS

LIST OF FIGURES

LIST OF TABLES

ACKNOWLEDGMENTS

I would like to express the deepest appreciation to my committee chair, Professor Lorenzo Valdevit, for the support and guidance provided throughout my time at UC Irvine. Our discussions were very valuable and essential for the development of my thesis. It was an honor to work as part of his research team and be on this continuous learning environment.

I would like to thank my committee members, Professor Tim Rupert and Professor J. Michael McCarthy, for the contributions to this work.

I thank the Institute for Design and Manufacturing Innovation at UCI for providing access and training in additive manufacturing techniques, especially to use the Stratasys Fortus 450mc to fabricate my samples. I also thank the Irvine Materials Research Institute and, in particular, the Laboratory for Eletron and X-Ray Instrumentation (LEXI), where I performed characterization of samples using the nano-CT-Scanner.

I thank all members of Mechanical of Materials and Structures Group for intellectual support and friendship.

I would like to acknowledge NSF for funding this work under Award #CCMI-1401496. Additional thanks to the Brazilian Science Without Borders Program and LASPAU for financial support, which allowed me to pursue my graduate studies at UC Irvine.

The Abaqus® Finite Element Analysis software is licensed from Dassault Systemes SIMULIA, as part of a Strategic Academic Customer Program between UC Irvine and SIMULIA. This support is gratefully acknowledged.

Finally, I would like to thank my family and friends for all the love and support.

ABSTRACT OF THE THESIS

The Effect of Manufacturing Defects on Compressive Strength of Polymeric Lattices Fabricated via Fused Deposition Modeling

By

Bianca Lis Rossi Dias Endo

Master of Science in Mechanical and Aerospace Engineering

University of California, Irvine, 2017

Professor Lorenzo Valdevit, Chair

Additive manufacturing is an emerging fabrication technology that has been incorporated into diverse industry segments, from aerospace to biomedical engineering. One of its key strengths is the ability to easily fabricate architected materials (e.g., lattices) with virtually any topology and over a wide range of dimensions. As the smallest dimension in the unit cell approaches the resolution of the equipment, though, significant defects get introduced, which have the potential to strongly affect the mechanical and functional properties of the architected material. Here, the effect of manufacturing defects on the compressive strength of solid lattices produced by Fused Deposition Modeling (FDM) in polycarbonate is studied. The choice of this printing technology was dictated by the commercial penetration of FDM printers in most industrial sectors and the ready availability of FDM machines; polycarbonate was chosen as it is one of the most commonly used structural polymers for FDM.

A state-of-the-art commercially available 3D printer was used to fabricate a large batch of lattice samples, varying topology, bar diameter and aspect ratio. All samples were CT scanned to quantify external and internal defects, and subsequently mechanically tested in compression. Finite elements models were built for the CT-derived lattices and the results compared with the lattice compression experiments. Once the numerical models were validated, the defect sensitivity of these lattices was quantified by comparing the FE strength predictions for nominally perfect and CT-derived lattices. This defect sensitivity was correlated to geometrical dimensions, failure mechanism and lattice topology.

1. INTRODUCTION AND MOTIVATION

Humans have looked at nature for answers to problems along our existence [1]. This makes a lot of sense, since life has evolved well-adapted structures and materials over billions of years by natural selection.

Cellular materials can be found in many applications in nature, where high strength and low density are needed. Birds, for example, need to be as light as possible in order to fly without getting tired. To achieve this, all flying birds have hollow bones, filled with pockets of air. The bones are held together by thin bar-like structures called struts. The struts prevent the bones from collapsing inward.

Figure 1: Cellular material in the core of a bird bone [2].

The architecture of a bird bone core is complex, with intricately shaped ligaments and variations in density. Although scientists and engineers have developed materials that are superior to the biologic based materials, the cellular architectures developed by humans are much less sophisticated than nature's [3]. This was limited by constraints in traditional manufacturing technologies until some years ago.

The advances in additive manufacturing technologies, which allow the manufacture of complex parts directly from three-dimensional CAD models, have been enabling fabrication of cellular materials with more complex architectures [4][5][6]. In addition to it,

computational methods have improved enough to empower the design of new structures and materials [7][8].

Nevertheless, other manufacturing difficulties emerge with additive manufacturing techniques [9]. For the fabrication of cellular materials and microstructures, the challenges are related to the time spent during the fabrication and quality of the structure as the dimensions get close to the equipment resolution. As the smallest dimension in the cellular material approaches the resolution of the equipment, significant defects get introduced. These defects have the potential to strongly affect the mechanical and functional properties of the architected material.

In the present work, the effect of manufacturing imperfections on solid architected materials fabricated via additive manufacturing technique is investigated. These defects change the strength of the structures, and will define if the material is appropriate for applications that require structural integrity.

2. BACKGROUND

This chapter provides some relevant background in cellular materials and their deformation modes, as well as an overview of additive manufacturing techniques, specifically the one used for this work.

2.1 Cellular materials

Cellular solids are made up of an interconnected network of solid struts or plates, forming the edges and faces of the cells [10]. They have been investigated for a variety of applications, from the ones that require structural strength to thermal insulation and impact protection, among others [11][12][13][14][15].

Materials with cellular structure widely occur in nature; examples are wood, bones, cork, glass sponges and bird beaks [16]. Scientists and engineers have made many artificial cellular structures, such as stochastic foams [17][18] and honeycomb-like materials [19] used for lightweight aerospace components.

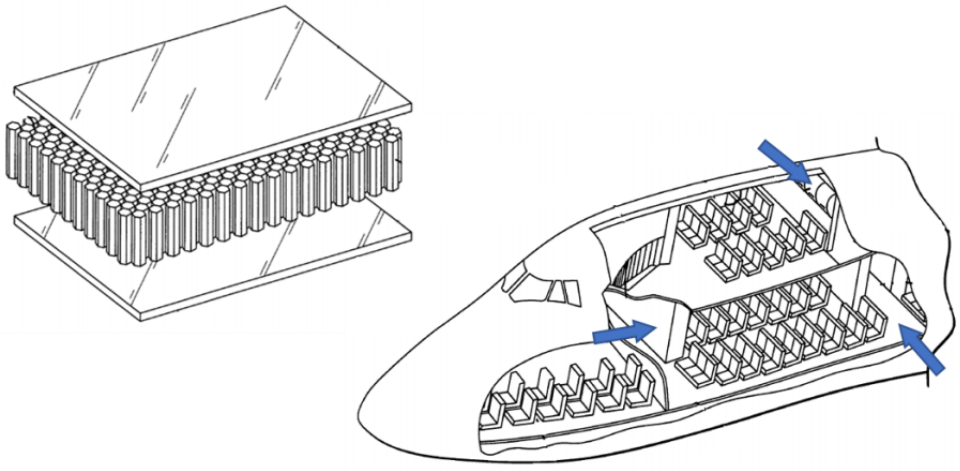

Figure 2: Honeycomb structure and applications in an airplane: floor, walls and overhead bin. Adapted from [20].

Man-made cellular materials have added architecture, increasing the mechanical efficiency of structures [21]. Architecture provides an additional degree of freedom in the design of a material and is possible due to the advances in computation and the progress in additive manufacturing technologies [7].

Figure 3: Nickel microlattice, example of architected material [22].

Most applications of cellular materials cause them to be loaded in compression [23]. Their elastic modulus (E) and strength (σ) can be calculated analytically and thru uniaxial compression tests.

An important structural characteristic of a cellular solid is its relative density ($\bar{\rho}$), defined as the density of the structure (ρ^*) divided by the density of the solid of which is made (ρ_s). E and σ follow the typical scaling relationships [10]:

$$\frac{E}{E_s} = \beta \bar{\rho}^b \tag{1}$$

$$\frac{\sigma}{\sigma_s} = \gamma \bar{\rho}^c \tag{2}$$

where E_s and σ_s are the elastic modulus and the strength of the solid material, respectively. β, γ, b and c are non-dimensional parameters of order 1 that depend on the architecture.

2.2 Bending VS stretching dominated architectures

Under compression, cellular solids deform by bending and stretching of the cell walls. The topology of the structure will dictate which mechanism dominates the deformation. Figure 4 illustrates a representative unit cell configuration for the two cases.

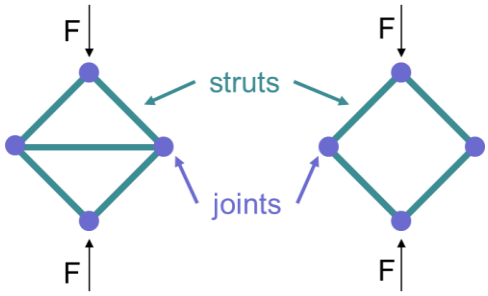

Figure 4: Schematic of unit cells for stretching (left) and bending (right) dominated lattice materials. Adapted from [24].

The joints are assumed welded and prevent free rotation of the struts. The structure on the left is stretching dominated. When loaded as shown, the diagonal struts deform primarily by axial compression, whereas the horizontal strut deforms axially in tension. When the strength of the material is exceeded, the struts will generally suddenly collapse by fracture or buckling (elastic or plastic). For the bending dominated structure on the right, the applied load would induce bending moments on the joints, causing the struts to deform primarily by bending, with generally negligible axial stress [24]. Failure will occur by progressive spreading of plasticity in the members, possibly followed by fracture.

Bending dominated structures have their elastic modulus (E) proportional to the relative density squared ($\bar{\rho}^2$), and a yield strength (σ_y) that scales with ($\bar{\rho}^{1.5}$) [25]. Stretching dominated structures have higher stiffness and strength, scaling linearly with the relative density [26]. This means that comparing a stretching and a bending dominated

structure with the same relative density, the first one has much higher elastic modulus and strength. Therefore, stretching dominated structures are the best choice for lightweight structural applications; however, because the deformation mechanisms involve "hard" modes (tension and compression) rather than "soft" ones (bending), initial yield is typically followed by plastic buckling or brittle collapse of the struts. Conversely, bending dominated structures deform more progressively after yielding by plastic bending of the members. This mode of deformation makes them preferable for applications that require energy absorption [27].

2.3 Additive manufacturing techniques

Additive manufacturing is the "process of joining materials to make objects from 3D model data, usually layer upon layer" [28]. It first emerged in the 1980s with stereolithography, a process that solidifies thin layers of ultraviolet light-sensitive liquid polymer using a laser [29].

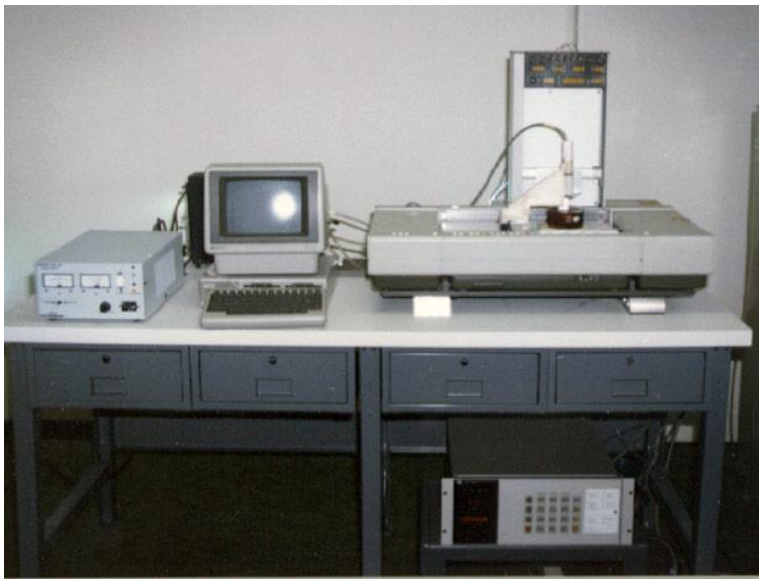

Figure 5: One of the first stereolithography machines ever made [30].

Thirty years later, additive manufacturing has become a mainstream manufacturing process. The advantages, compared to conventional manufacturing processes, are: material and resource efficiency, since it doesn't require auxiliary tools such as jigs, fixtures and cutting tools; part and production flexibility, because complex features can be made in only one piece straight [31].

The flexibility on the fabrication of complex parts is what makes additive manufacturing an excellent option to produce architected materials. Among the existing processes, the fused deposition modeling (FDM) technique [32][33] was chosen to produce the samples for this current work.

In the FDM process, liquid thermoplastic material is extruded from a movable head and then deposited in thin layers onto a substrate. The material is heated slightly above its melting point, so that it solidifies after extrusion and cold welds to the previous layers. Machines with two nozzles have also been developed, one for part material and the other for support material [34]. The support material can be removed from the part without damaging it.

Figure 6: Example of part printed with a different support material [35].

However, additive manufacturing technologies still have some drawbacks such as size limitations, imperfections on the final product and cost. The size limitations are related to the available envelope of the machine, that limits the maximum size of the parts produced. The minimum dimension of features is also limited, but by the resolution of the equipment. Imperfections often appear on rough and ribbed surface finish [36], and may be more frequent as the dimensions of the parts decrease.

3. OBJECTIVES

The main goal of this research is to investigate the effect of manufacturing defects on the compressive strength of solid lattices produced via fused deposition modeling (FDM). To accomplish the goal, the following objectives were established:

1 – Design and fabrication of lattice materials;

2 – Analysis of geometric imperfections in FDM lattices;

3 – Analytical calculation of lattice strength;

4 – Modeling of ideal lattices and lattices with defects;

5 – Mechanical characterization of lattice designs;

6 – Comparison of results.

4. METHODS AND PROCEDURES

This chapter describes the tasks performed, the equipment and software used to develop the research work.

4.1 Unit cell geometry

Two different unit cell topologies were chosen to be modeled using the software Solidworks [37]: the cross-truss unit cell and the octet-truss unit cell, illustrated below:

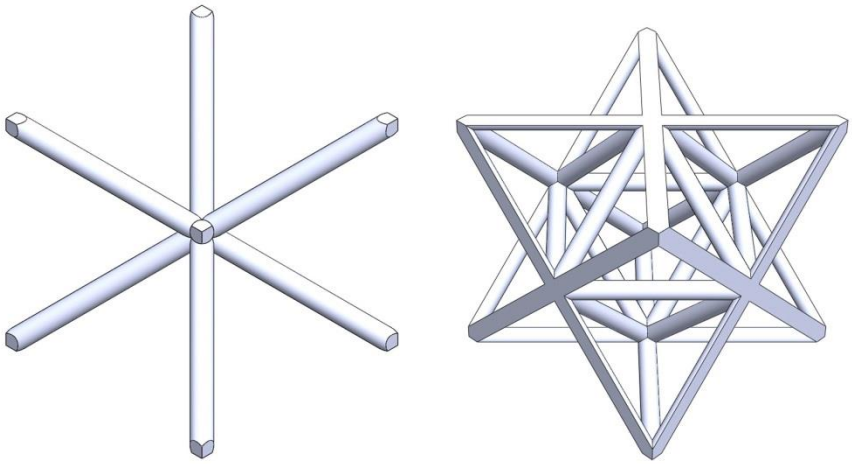

Figure 7: Cross-truss (left) and octet-truss (right) unit cells.

While the cross-truss unit cell is a bending dominated structure, the octet-truss unit cell deforms by stretching of the cell struts. An extensive body of literature exists on the mechanical properties of these two lattice structures [38][39][40][41][42][43][44] [45].

The diameter and the aspect ratio of the struts were used as variables in the design of the unit cells, as follows:

Table 1: Unit cells dimensions for the lattices investigated in this work.

Unit cell	Diameter (D)	Length (L)	Aspect ratio (L/D)
Octet-truss	1 mm	4 mm	4
	2 mm	8 mm	
	1 mm	10 mm	10
	2 mm	20 mm	
Cross-truss	1 mm	4 mm	4
	2 mm	8 mm	
	1 mm	10 mm	10
	2 mm	20 mm	

4.2 Samples fabrication

The samples were fabricated using the state-of-the-art Stratasys Fortus 450mc fused deposition modeling (FDM) machine [46]. The Fortus 450mc has a build envelope of 406 x 355 x 406 mm, and achievable accuracy of ±0.127mm or ±0.0015 mm/mm, whichever is greater. This system uses a wide range of thermoplastics with advanced mechanical properties. Polycarbonate was chosen for the samples fabrication, as it is one of the most commonly used structural polymers for FDM. It is widely used in automotive, aerospace and medical applications.

The software package Insight [47] was used to prepare the model to be manufactured on the Fortus system, by slicing it and generating support structures and material extrusion paths. Because of the complex geometry of the unit cells, a soluble material was chosen for the support structures. After being printed, the samples were

immersed in a solution of NaOH and water in a shaking bath at 65^{o}C, for dissolution of support material.

Figure 8: Stratasys Fortus 450mc fused deposition modeling 3D printer.

4.3 Determination of material properties

As the fused deposition modeling fabrication method builds parts by depositing thin lines of material in different directions, the produced parts usually exhibit considerably anisotropy, and their mechanical properties could be significantly different from those of parts molded from the same base material [48]. In order to understand the mechanical properties of the fabricated polycarbonate lattices and in particular the influence of the angle between the strut length and the printing direction, simple prismatic specimens were fabricated in three different deposition angles: 0^{o}, 45^{o} and 90^{o}, as illustrated in Figure 9.

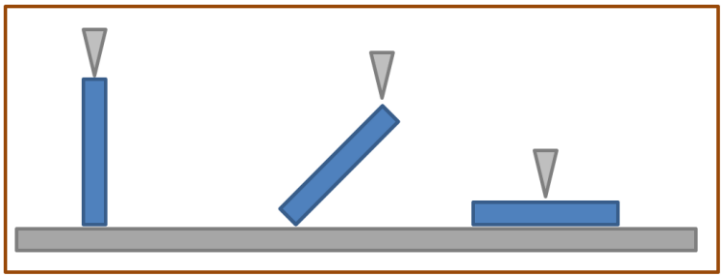

Figure 9: Bars printed at 0º (left), 45º (center) and 90º (right) relative to the printing direction (i.e., the z-axis of the printer). The arrow schematically represents the printer nozzle.

Uniaxial mechanical tests (tension and compression) were performed to capture the elastic modulus and strength of the bars. Figure 10 illustrates the procedure.

Figure 10: Tensile (left) and compressive (right) tests of a bar.

4.4 Determination of geometric imperfections via CT scanning

The printed samples were scanned using the three-dimensional X-ray Xradia VersaXRM™ 410 [49], showed in Figure 11. This non-destructive micro tomography test provides cross sections of the samples used to recreate a virtual model, capturing internal and external imperfections. Each sample took from one to three hours to be scanned, depending on sample dimensions and number of cross sections required per sample. The equipment provides a spatial resolution of up to 900 nm, determined by the size of the

samples. The software Simpleware [50] was used to process the data acquired and generate the 3D model and mesh of these samples.

Figure 11: X-ray CT scanner Xradia VersaXRM™ 410.

4.5 Analytical formulation of yielding and buckling strength

Analytical models for yielding and buckling strength were used to predict the strength of the unit cells in this study. The geometric parameters required to fully define the analytical yield strength are the unit cell angle (θ), length (l) and diameter (D) of the struts, illustrated in Figure 12.

The compressive strength along the z direction of the cross-truss and octet-truss lattices can be estimated by beam theory considerations. When uniaxially compressed by a load P, the load distribution occurs in the unit cells as schematically indicated in Figure 13.

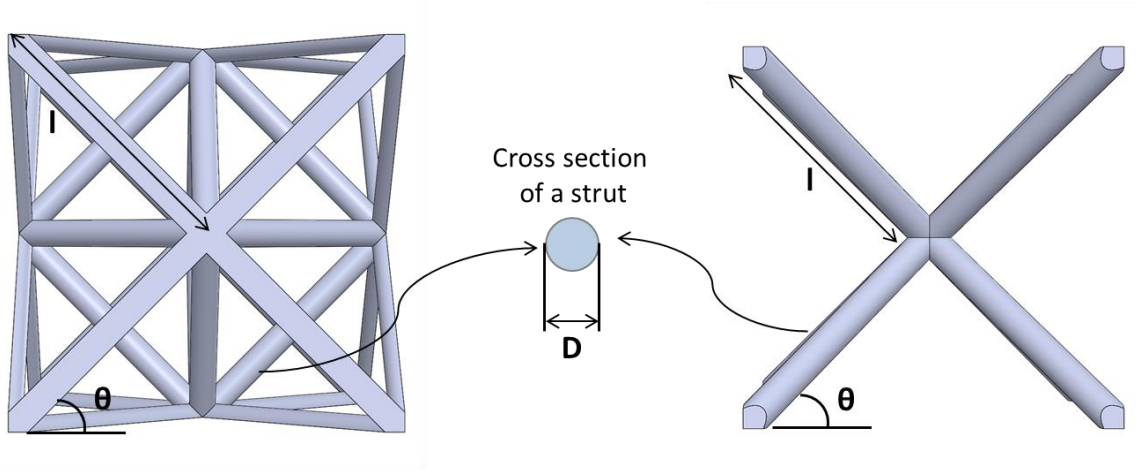

Figure 12: Geometry of the octet-truss lattice (left) and the cross-truss lattice (right) and variables definition.

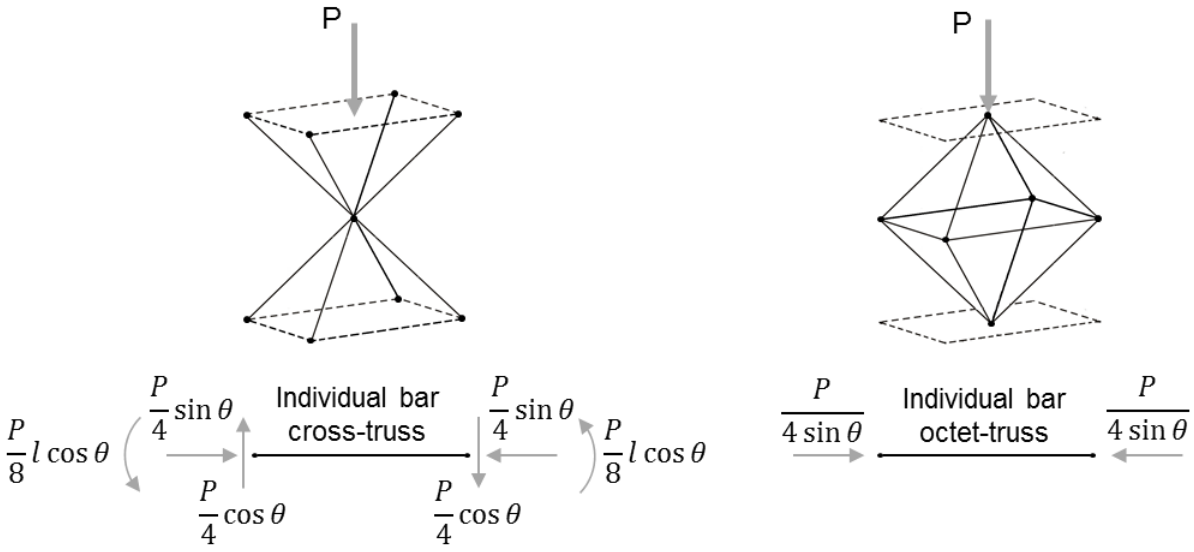

Figure 13: Schematic of a unit cell under compression (cross-truss on the left and octet-truss on the right) and free-body diagram of a single bar

In the cross-truss unit cell, each bar is subjected to a uniform compression force and a linearly varying bending moment, maximum M_{max} at the nodes. From the free body diagram in Figure 13 (left), the maximum stress in the bar is:

$$\sigma_{max} = \frac{M_{max}}{I}\frac{D}{2} + \frac{P\sin\theta}{4A} = \frac{4Pl\cos\theta}{\pi D^3} + \frac{P\sin\theta}{\pi D^2} \quad , \tag{3}$$

where A and I are the area and the moment of inertia of a bar member, respectively. By equating the maximum stress in the bar to the yield strength of the constituent material $\sigma_y{}^0$, and noticing that the load P acts on a unit cell of area $2l^2(\cos\theta)^2$ [38], the effective yield strength of the cross-truss lattice can be expressed as:

$$\frac{\sigma_y}{\sigma_y{}^0} = \frac{\pi\left(\frac{D}{l}\right)^3}{8\left[(\cos\theta)^3\left(1+\frac{\tan\theta}{4}\frac{D}{l}\right)\right]} \quad . \tag{4}$$

Collapse of cross-truss lattice can also occur by elastic buckling. The buckling load can be estimated by equating the normal force in each bar to the Euler buckling load [51] for a simply supported column:

$$\frac{P}{4}\sin\theta = \frac{\pi^2 EI}{K^2 l^2} \;\rightarrow\; P = \frac{\pi^3 ED^4}{16l^2\sin\theta} \quad , \tag{5}$$

where K is equals to 1 for a bar with pinned ends.

The effective global buckling strength for the cross-truss lattice then can be expressed as:

$$\frac{\sigma_{Eb}}{\sigma_y{}^0} = \frac{\pi^3\left(\frac{E}{\sigma_y{}^0}\right)\left(\frac{D}{l}\right)^4}{32(\cos\theta)^2\sin\theta} \quad . \tag{6}$$

For the octet-truss unit cell the procedure is similar. From the free body diagram in Figure 13, the maximum stress in the bar is:

$$\sigma_{max} = \frac{\frac{P}{4\sin\theta}}{\frac{\pi D^2}{4}} = \frac{P}{\pi D^2\sin\theta} \quad , \tag{7}$$

By equating the maximum stress in the bar to the yield strength of the constituent material $\sigma_y{}^0$, and noticing that the load P acts on a unit cell of area $2l^2 (\cos\theta)^2$, the effective yield strength of the octet-truss lattice can be expressed as:

$$\frac{\sigma_y}{\sigma_y{}^0} = \frac{\pi \sin\theta \left(\frac{D}{l}\right)^2}{2(\cos\theta)^2} \quad . \tag{8}$$

Collapse of octet-truss lattice can also occur by elastic buckling. The buckling load can be estimated by equating the normal force in each bar to the Euler buckling load for a simply supported column, leading to:

$$\frac{P}{4\sin\theta} = \frac{\pi^2 EI}{K^2 l^2} \;\rightarrow\; P = \frac{\pi^3 E D^4 \sin\theta}{4l^2} \quad . \tag{9}$$

where K is equals to 0.5 for a bar with fixed ends.

Table 2 summarizes the analytical models for yielding strength and buckling strength of the octet-truss and cross-truss unit cells.

Table 2: Analytical models for yielding and buckling strength of Octet-truss and Cross-truss unit cells.

Unit cell	**Yield Strength**	**Buckling Strength**
Octet-truss	$\frac{\pi \sin\theta \left(\frac{D}{l}\right)^2}{2(\cos\theta)^2}$	$\frac{\frac{E}{\sigma_y}\pi^3 \sin\theta \left(\frac{D}{l}\right)^4}{8(\cos\theta)^2}$
Cross-truss	$\frac{\pi \left(\frac{D}{l}\right)^3}{8\left[(\cos\theta)^3\left(1+\frac{\tan\theta}{4}\frac{D}{l}\right)\right]}$	$\frac{\frac{E}{\sigma_y}\pi^3 \left(\frac{D}{l}\right)^4}{32(\cos\theta)^2 \sin\theta}$

4.6 Numerical model of strength of ideal and CT-scanned cells

4.6.1 Meshing

Two finite element models were generated for each unit cell. The first model was based on the geometry designed on Solidworks and called “perfect model”. The perfect models meshes were created using the software Abaqus [52]. The second model was generated based on the Nano-CT-Scanned images of the printed samples, using the software Simpleware. These models are called “CT-Scanned models”.

4.6.2 Boundary conditions

The boundary conditions are a critical aspect on the finite element model configuration. Throughout this work, periodic boundary conditions were used to ensure the results were applicable to a large system (i.e. multiple-cell samples). The configuration models a uniaxial compression test. Firstly, the six plane surfaces of the unit cells were constrained so that they remained plane at all times. Secondly, all nodes on the –x, -y and –z faces on the unit cell were prevented from translating and rotating. The nodes on +x and +y faces were allowed to move along x and y, respectively. Finally, the nodes on +z face were subject to a downward displacement or force. Figure 14 illustrates this configuration.

For all simulations, isotropic linear elastic perfectly plastic properties were used for the solid material, extracted from the material compressive and tensile tests discussed in Section 4.3. Quasi-static simulations were performed on all unit cells. For the unit cells that were predicted to fail by elastic buckling according to the analytical models, buckling simulations (i.e., eigenvalue extractions) were also performed. The dominant buckling mode was added as an imperfection for the static simulations.

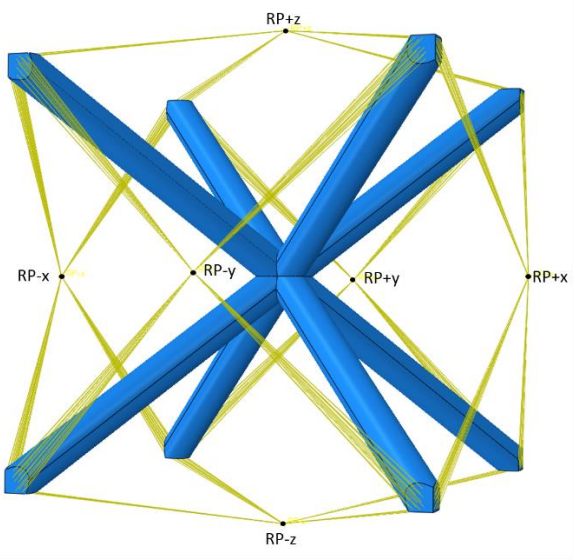

Figure 14: Example of unit cell with schematic depiction of the boundary conditions imposed in the FE simulations: nodes connected by yellow lines are coupled to their respective reference node (RP) in all rotational degrees of freedom. Additionally, nodes connected to RP±x, RP±y and RP±z are coupled in the x-displacement, y-displacement and z-displacement respectively. The reference points RP-x, RP-y and RP-z are maintained at x=0, y=0 and z=0 respectively. RP+x and RP+y are free to move along x and y respectively, and vertical displacements are specified at RP+z.

In addition to the quasi-static simulations, a density analysis was performed on the models, in order to compare the density of the ideal cells with the density of the CT-scanned cells.

4.7 Compression tests

To experimentally characterize the mechanical properties of the samples, uniaxial compression experiments were performed. All tests were performed with a servo-electric INSTRON 8862 frame (illustrated in Figure 15), equipped with a FastTrack 8800 control system and a National Instrument SCXI data acquisition system. The load was measured

using the frame load cell and the displacement was computed using the linear variable displacement transducer (LDVT), embedded in the frame actuator. All tests were displacement-rate controlled. The effective stress in the lattice was calculated by dividing the applied load by the area of the lattice sample, and the effective strain by dividing the cross-head displacement by the original length of the sample. Results were presented in the form of effective stress-strain curves for each sample.

Figure 15: INSTRON 8862 used to perform the tests (left) [53] and sample being tested (right).

5. RESULTS

5.1 Mechanical properties of the base material

For each deposition angle, three identical prismatic samples (8 mm length x 2 mm diameter) were tested both in compression and in tension at a displacement rate of 0.05 mm/s. Representative stress-strain curves obtained on the compressive and tensile tests of the bars are summarized in Figure 16. The tensile strength has a stronger dependence on the layer deposition direction compared to the compressive strength. The bars show a brittle behavior under tension, while are more ductile under compression.

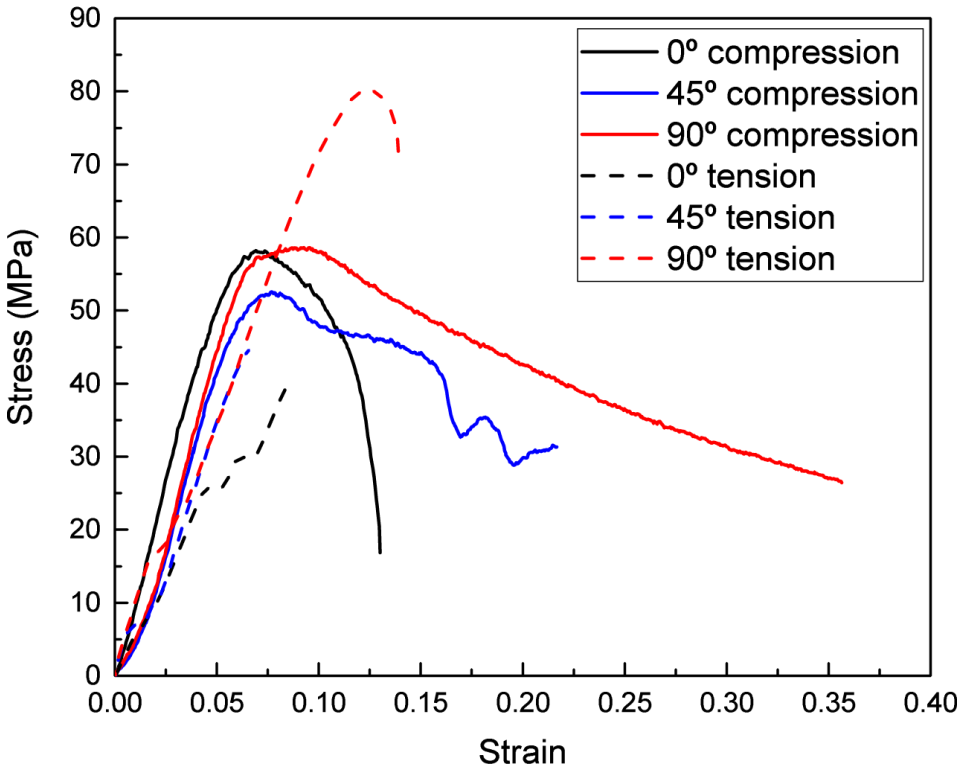

Figure 16: Experimental stress-strain curves of the compression and tension specimens used for materials characterization.

Table 3 and Table 4 summarize the average strength and elastic modulus, along with the standard deviation obtained on the tests.

Table 3: Material properties obtained on the compression test of specimens.

Specimen deposition angle	Average strength	Average elastic modulus
0^o	1203±55 MPa	62±10 MPa
45^o	1174±55 MPa	56±4 MPa
90^o	1329±107 MPa	59±0 MPa

Table 4: Material properties obtained on the tension test of specimens.

Specimen deposition angle	Average strength	Average elastic modulus
0^o	678±32 MPa	41±0 MPa
45^o	743±135 MPa	40±5 MPa
90^o	965±77 MPa	92±10 MPa

Based on these results, an average elastic modulus of 1.3 GPa and a strength of 55 MPa were extracted and used in all the analytical models and the numerical simulations on the lattices. The choice of using compression data (as opposed to tensile data) stems from the fact that all bars (with the exception of the horizontal bars in the octet lattices) are subjected to compressive stresses during lattice-level compression; we then expect the compressive properties to dominate the mechanical response. The accuracy of this assumption is discussed when experimental results are compared with analytical/numerical predictions.

5.2 Fabricated lattices

The fabricated lattices are illustrated in Figure 17. For the structures with unit cells that had aspect ratio equals to 4 ((a), (b), (e) and (f) in Figure 17), the samples were designed with 5 x 5 x 5 unit cells. Sample (c) had 3 x 3 x 3 unit cells, (g) had 4 x 4 x 4 unit cells and (d) and (h) had 2 x 2 x 2 unit cells. These size differences are due to the limitations in maximum dimensions for sample analysis using the nano-CT-Scan equipment.

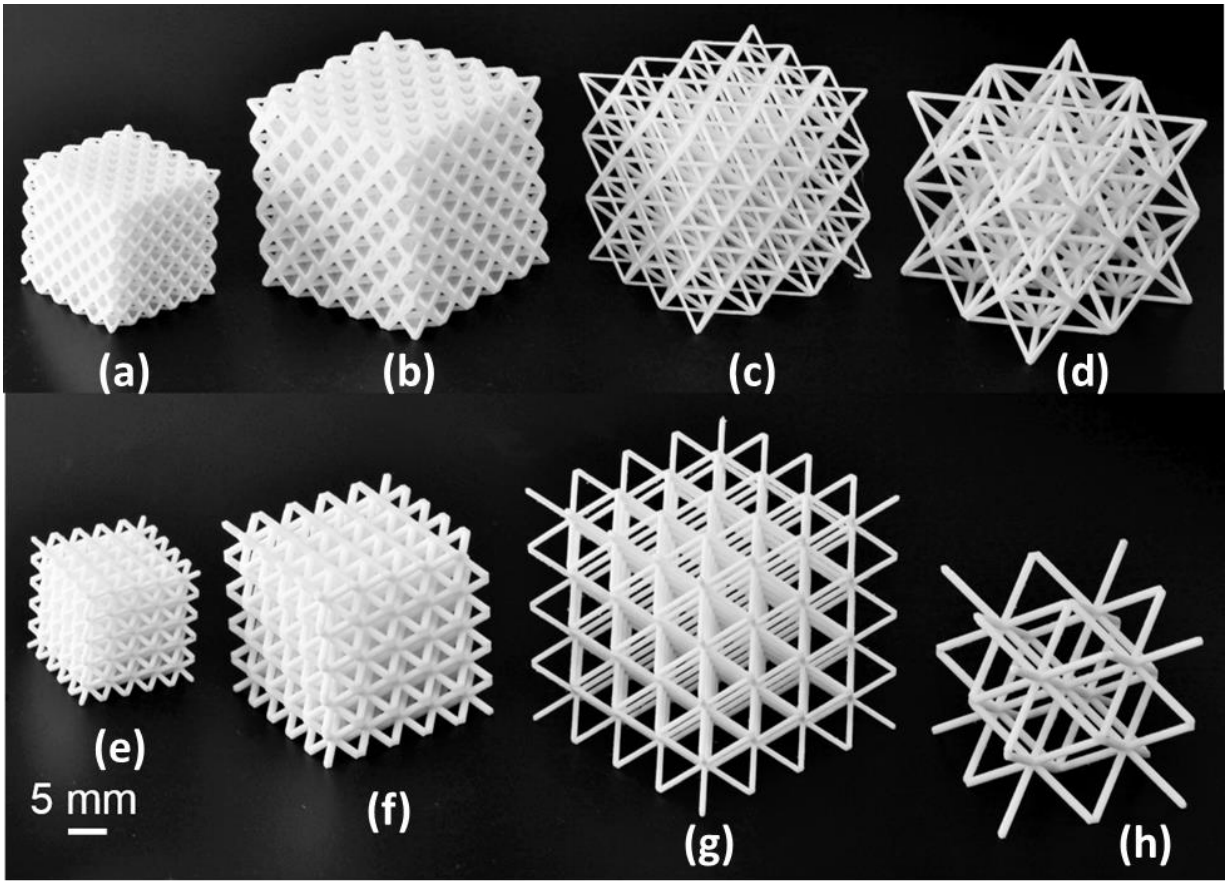

Figure 17: Lattice samples fabricated in polycarbonate via FDM – (a) octet-truss 4 mm length x 1 mm diameter struts; (b) octet-truss 8 mm length x 2 mm diameter struts; (c) octet-truss 10 mm length x 1 mm diameter struts; (d) octet-truss 20 mm length x 2 mm diameter struts; (e) cross-truss 4 mm length x 1 mm diameter struts; (f) cross-truss 8 mm length x 2 mm diameter

struts; (c) cross-truss 10 mm length x 1 mm diameter struts; (d) cross-truss 20 mm length x 2 mm diameter struts.

Table 5 shows the manufacturing time for each sample using the Fortus 450mc.

Table 5: Fabrication time for all lattice samples.

Unit cell	Diameter	Length	Fabrication time
Octet-truss	1 mm	4 mm	11 h
	2 mm	8 mm	45 h
	1 mm	10 mm	56 h
	2 mm	20 mm	40 h
Cross-truss	1 mm	4 mm	4 h
	2 mm	8 mm	24 h
	1 mm	10 mm	23 h
	2 mm	20 mm	58 h

5.3 Comparison of ideal and CT-scanned lattice geometries

The following images illustrate the designed unit cells and the 3D reconstruction of the printed samples made using the software Simpleware. The cross-truss unit cells are represented in Figure 18, Figure 19 and Figure 20; the octet-truss unit cells are represented in Figure 21, Figure 22 and Figure 23.

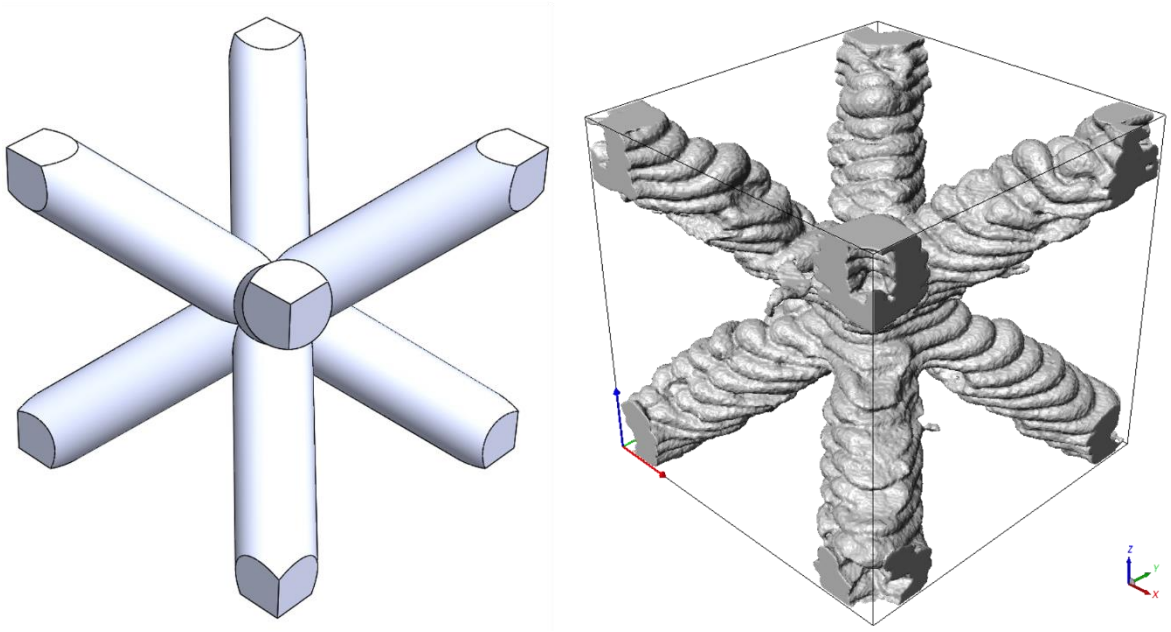

Figure 18: Cross-truss unit cell – Ideal model (left) and CT-Scan model (right). Struts dimension: 4 mm length x 1 mm diameter.

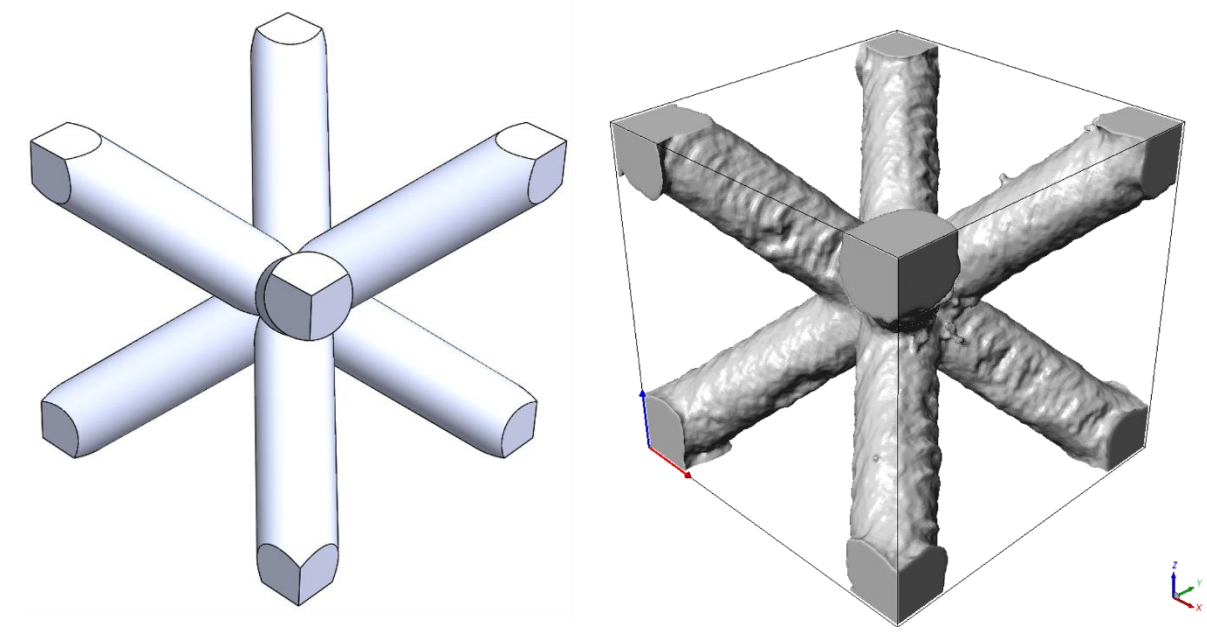

Figure 19: Cross-truss unit cell – Ideal model (left) and CT-Scan model (right). Struts dimension: 8 mm length x 2 mm diameter.

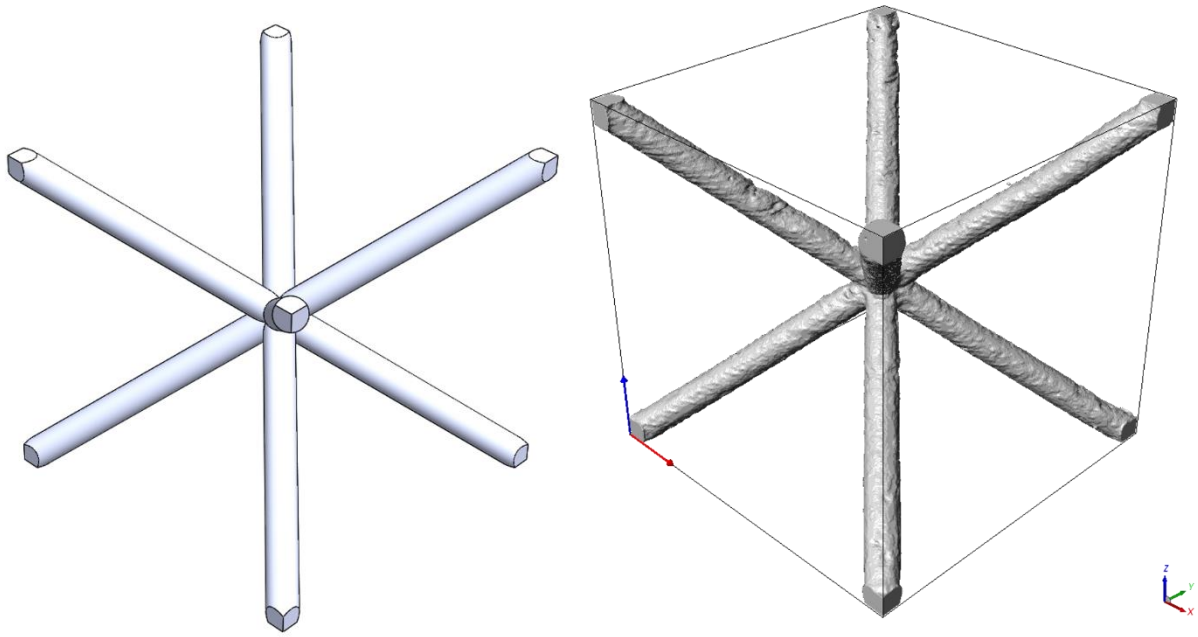

Figure 20: Cross-truss unit cell – Ideal model (left) and CT-Scan model (right). Struts dimension: 20 mm length x 2 mm diameter.

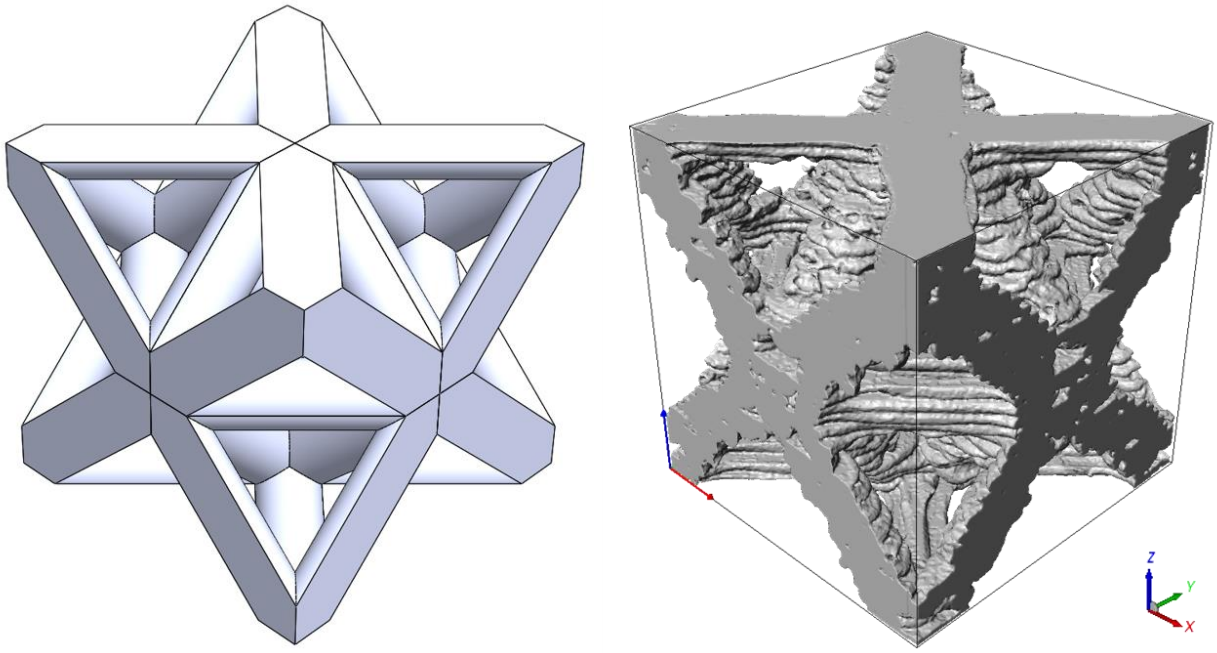

Figure 21: Octet-truss unit cell – Ideal model (left) and CT-Scan model (right). Struts dimension: 4 mm length x 1 mm diameter.

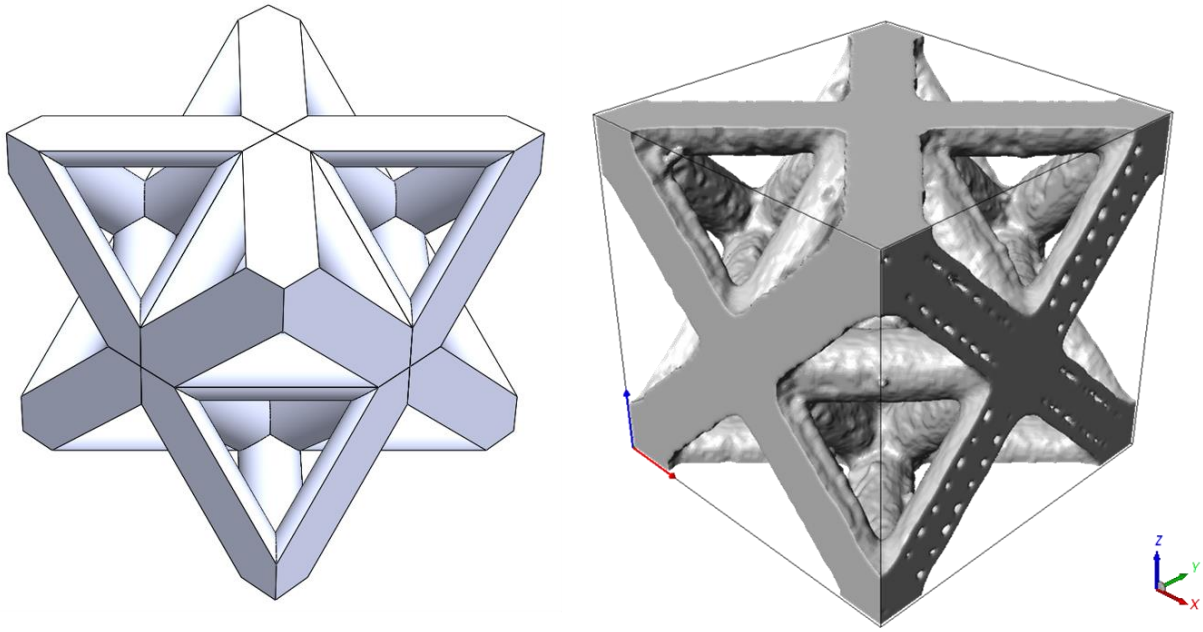

Figure 22: Octet-truss unit cell – Ideal model (left) and CT-Scan model (right). Struts dimension: 8 mm length x 2 mm diameter.

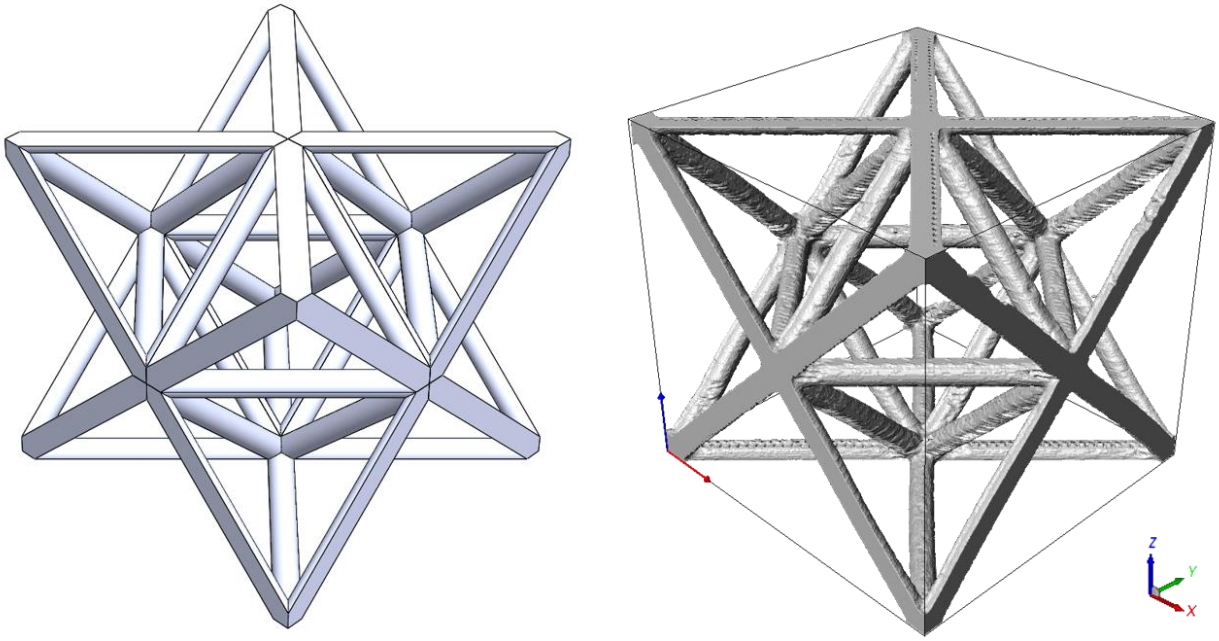

Figure 23: Octet-truss unit cell – Ideal model (left) and CT-Scan model (right). Struts dimension: 20 mm length x 2 mm diameter.

Figure 18 shows the cross-truss unit cell with 4 mm length x 1 mm diameter struts. The 3D reconstructed model shows the presence of voids in the interior of the struts, mainly in the area of the nodes. The surface is very irregular, and the separation of the printed layers can be seen clearly. Fewer imperfections on the surface are observed when the diameter of the struts increases to 2 mm, as illustrated in Figure 19 and Figure 20.

For the octet-truss lattices the effects of bar dimensions are similar. Figure 21 illustrates the octet-truss unit cell with 4 mm length x 1 mm diameter struts. The imperfections are seen both on the surface and in the interior of the bars. Specimen with thicker bars (Figure 22 and Figure 23) show fewer imperfections on the surface, but more voids inside of the bars.

The samples with aspect ratio 10 and diameter of the struts equals to 1 were more affected by the manufacturing imperfections. A few bars of these samples were lost during the removal of the support material, even when a soluble support material was used. The cross-truss sample lost more bars than the octet-truss, as the octet-truss unit cell has more connections between the bars.

The relative density of the unit cells were calculated based on the Ideal and CT-Scanned models. The results are summarized in the Table 6.

Table 6: Density of the unit cells.

Unit cell	Diameter (D)	Length (L)	Density of the Ideal model	Density of the CT-Scanned model	Ratio between CT-Scanned and Ideal model densities
Octet-truss	1 mm	4 mm	3.7×10^{-4} g/cm^3	3×10^{-4} g/cm^3	0.81
	2 mm	8 mm	3.7×10^{-4} g/cm^3	3.9×10^{-4} g/cm^3	1.05
	1 mm	10 mm	7.1×10^{-5} g/cm^3	N/A	N/A
	2 mm	20 mm	7.1×10^{-5} g/cm^3	6.9×10^{-5} g/cm^3	0.97
Cross-truss	1 mm	4 mm	2.4×10^{-4} g/cm^3	2.3×10^{-4} g/cm^3	0.94
	2 mm	8 mm	2.4×10^{-4} g/cm^3	2.9×10^{-4} g/cm^3	1.2
	1 mm	10 mm	4.5×10^{-5} g/cm^3	N/A	N/A
	2 mm	20 mm	4.5×10^{-5} g/cm^3	4.3×10^{-5} g/cm^3	0.95

5.4 Analytical predictions

The aspect ratio of the struts in the unit cells determines whether the lattice material will fail first by yielding or elastic buckling. Table 7 shows the analytical model results for relative strength of all unit cells (relative strength = lattice strength / yield strength of parent material). The values in bold represent the dominant failure mechanism for each cell.

The analytical models reveal that all cross-truss samples would fail by yielding, while the octet-truss samples with aspect ratio of 10 would fail by elastic buckling. This prediction is going to be confirmed by finite element modeling and experimental characterization.

Table 7: Analytical strength of the unit cells.

Unit cell	Diameter (D)	Length (L)	Analytical buckling strength	Analytical yield strength
Octet-truss	1 mm	4 mm	0.5061	**0.1388**
	2 mm	8 mm		
	1 mm	10 mm	**0.0129**	0.0222
	2 mm	20 mm		
Cross-truss	1 mm	4 mm	0.2531	**0.0163**
	2 mm	8 mm		
	1 mm	10 mm	0.0064	**0.0011**
	2 mm	20 mm		

5.5 Numerical (finite elements) predictions

This section shows the results of all finite element simulations performed on the lattice unit cells. Figure 24, Figure 25, Figure 26 and Figure 27 illustrate the stress-strain curves under uniaxial compression of the cross-truss unit cell with different dimensions and aspect ratios, where (a) is the ideal cell and (b) is the reconstruction of the printed sample. Contour plots of equivalent stress at selected points in the test are depicted to allow comparison of stress evolution between ideal and CT-scanned geometries. In all cases, a stress concentration is clearly seen at the nodes where the struts connect.

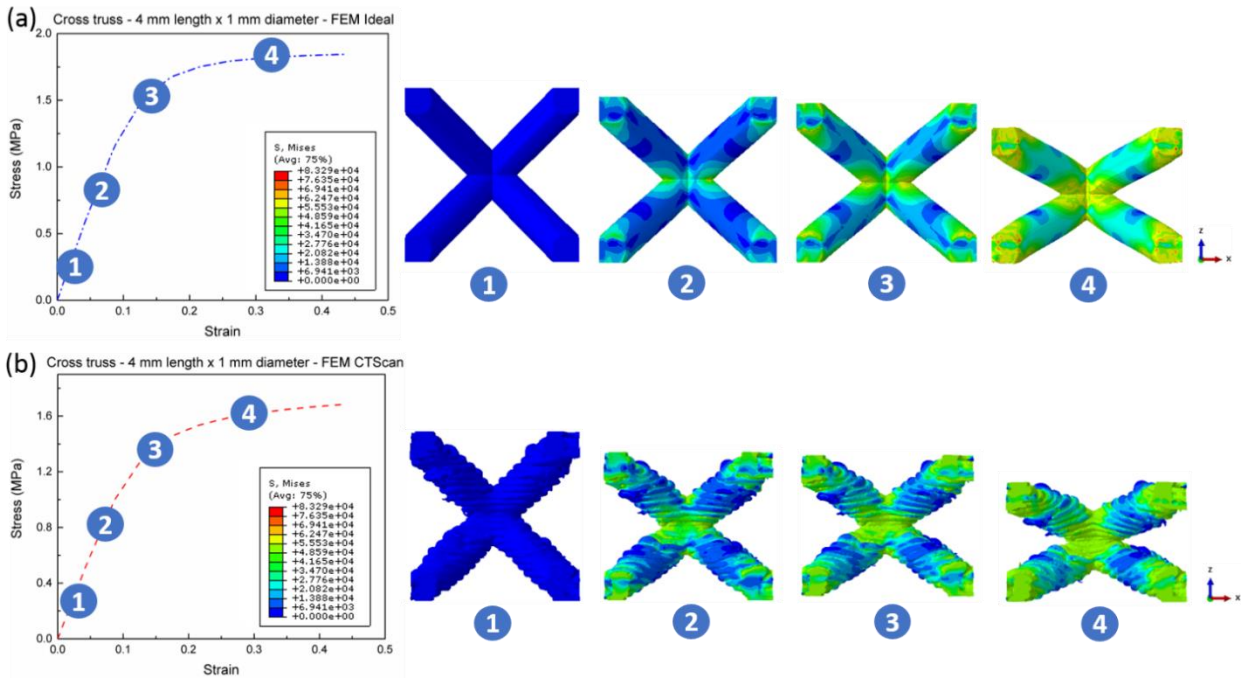

Figure 24: Stress-strain curve of the uniaxial compression simulation – Cross-truss 4 mm length x 1 mm diameter – (a) Ideal model and (b) CT-Scanned model.

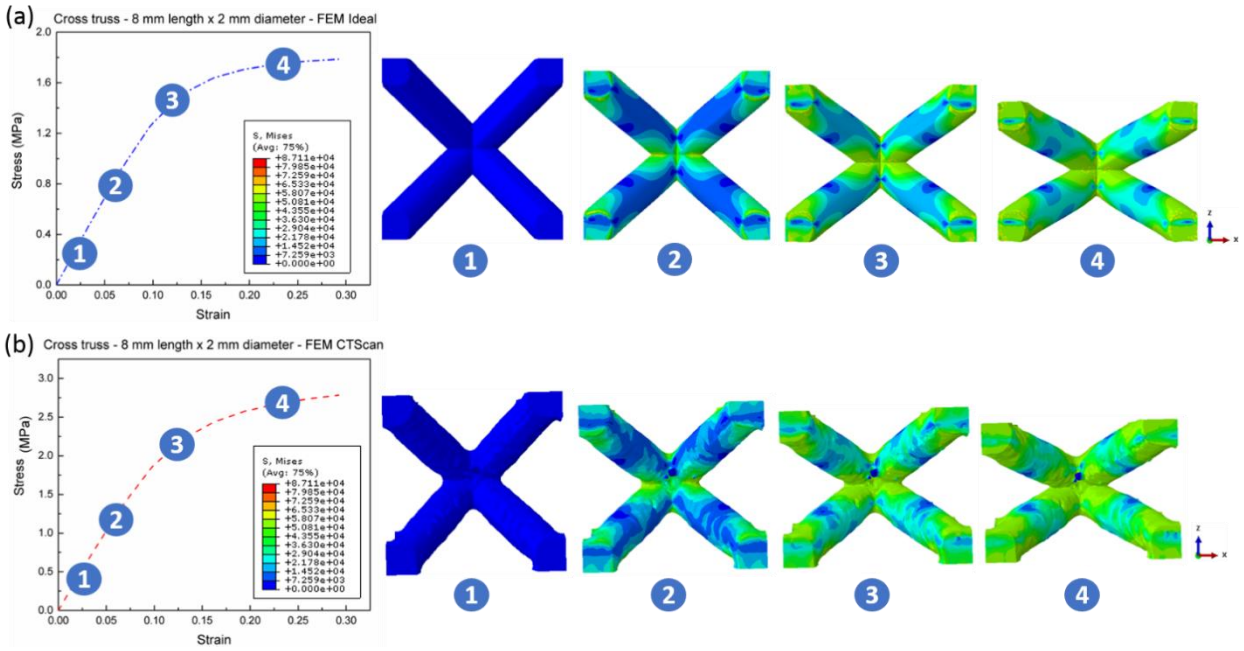

Figure 25: Stress-strain curve of the uniaxial compression simulation – Cross-truss 8 mm length x 2 mm diameter – (a) Ideal model and (b) CT-Scanned model.

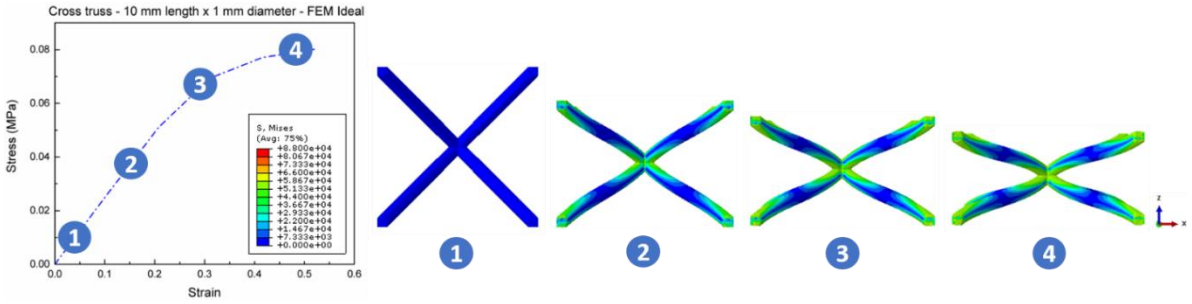

Figure 26: Stress-strain curve of the uniaxial compression simulation – Cross-truss 10 mm length x 1 mm diameter – Ideal model.

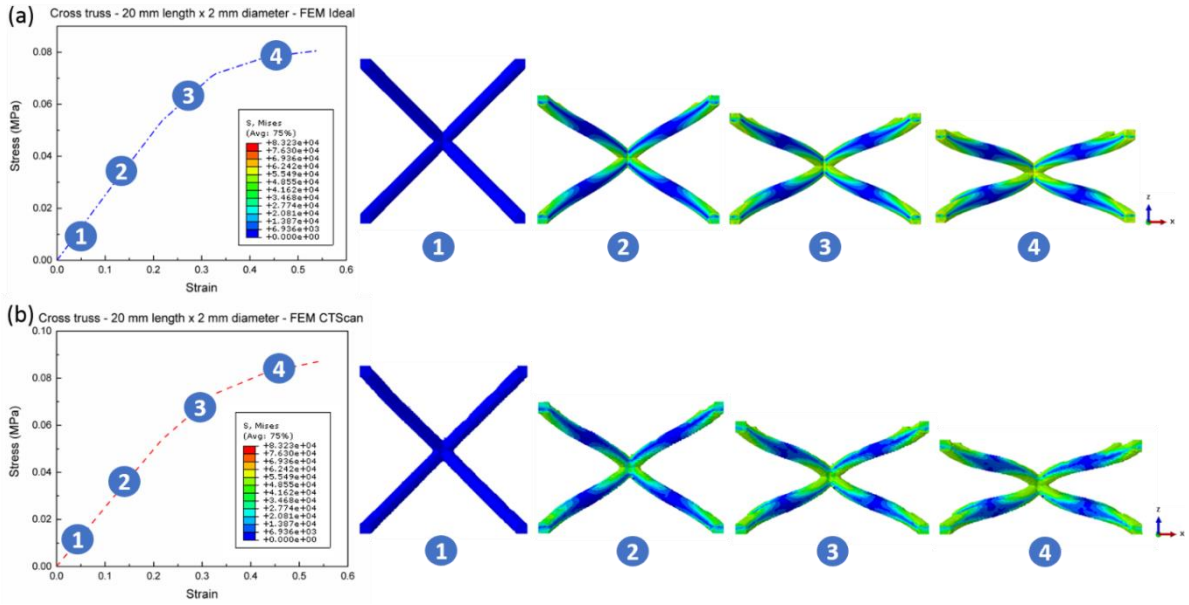

Figure 27: Stress-strain curve of the uniaxial compression simulation – Cross-truss 20 mm length x 2 mm diameter – (a) Ideal model and (b) CT-Scanned model.

Figure *28*, Figure 29, Figure 30 and Figure 31 present the same results for the octet-cell lattices. For the octet-truss cells, the stress concentration is less pronounced (see Figure 28 and Figure 29). According to the analytical models reported in the previous section, the octet-truss cells with aspect ratio 10 should fail first by buckling. This was also verified by eigenvalue extraction in finite elements analyses, and the dominant buckling

mode was included as an imperfection in the quasi-static simulations presented in Figure 30 and Figure 31.

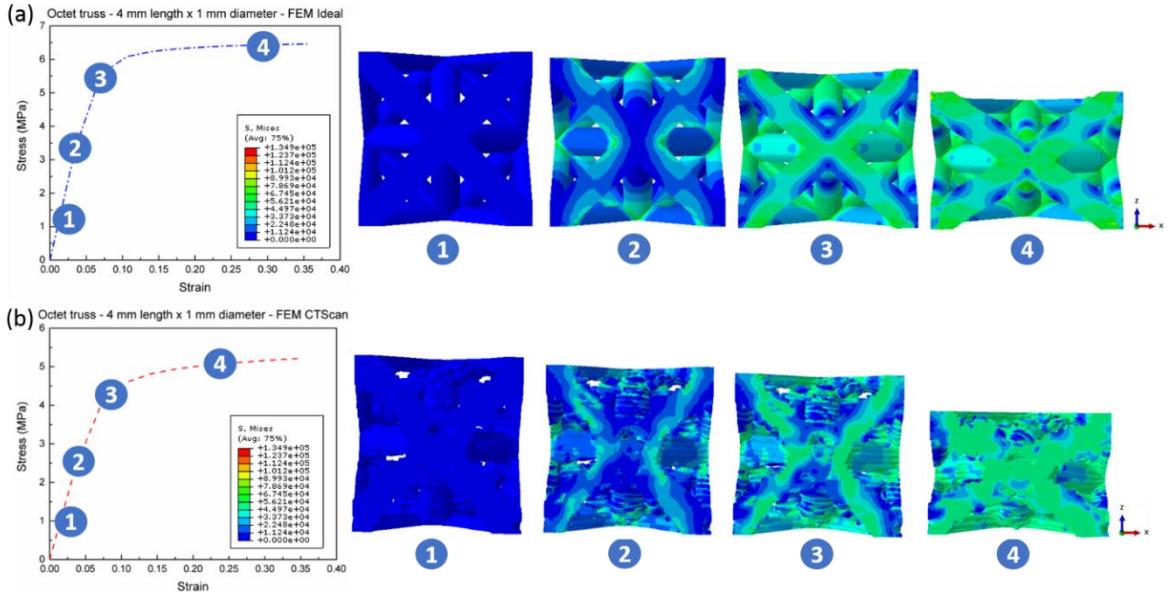

Figure 28: Stress-strain curve of the uniaxial compression simulation – Octet-truss 4 mm length x 1 mm diameter – (a) Ideal model and (b) CT-Scanned model.

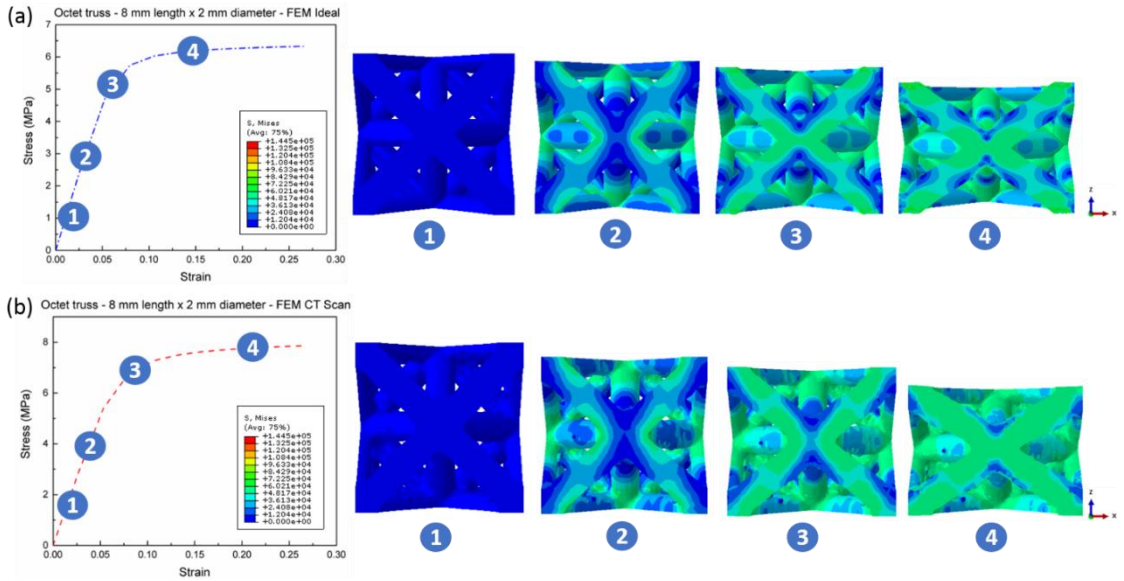

Figure 29: Stress-strain curve of the uniaxial compression simulation – Octet-truss 8 mm length x 2 mm diameter – (a) Ideal model and (b) CT-Scanned model.

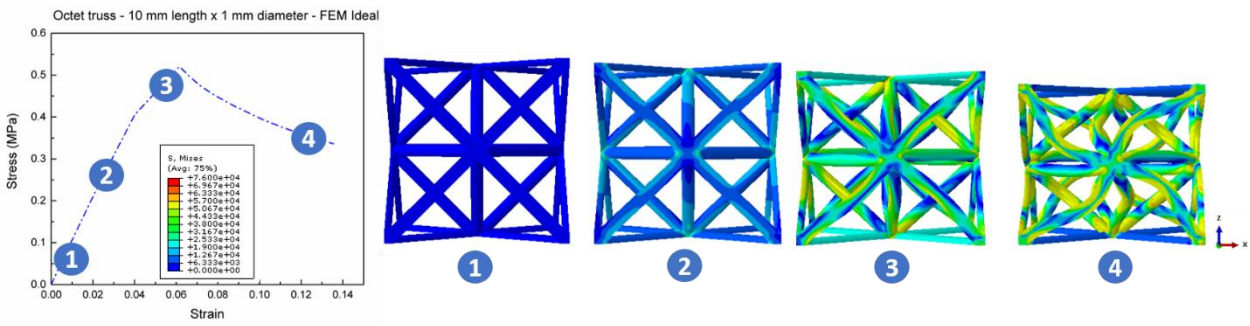

Figure 30: Stress-strain curve of the uniaxial compression simulation – Octet-truss 10 mm length x 1 mm diameter – Ideal model.

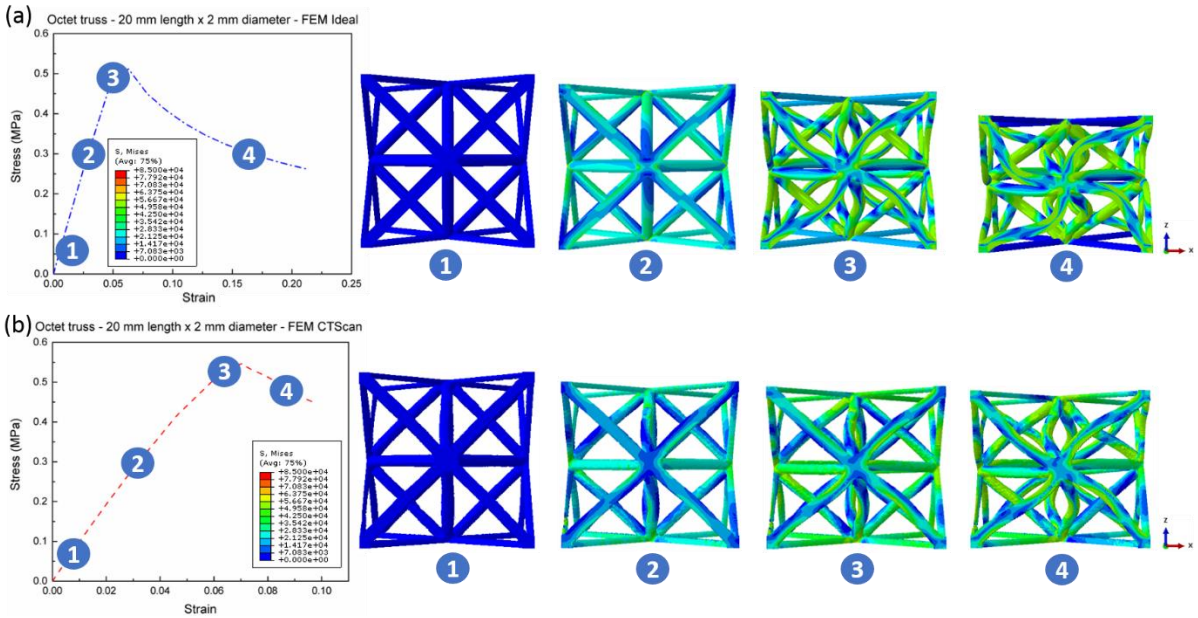

Figure 31: Stress-strain curve of the uniaxial compression simulation – Octet-truss 20 mm length x 2 mm diameter – (a) Ideal model and (b) CT-Scanned model.

5.6 Results from experimental tests

This section shows the results of the compression tests in the form of effective stress-strain curves. Sample images at various stages of compression are also reported to better illustrate the deformation and failure mechanisms. The cross-cell sample results are

presented in Figure 32, Figure 33, Figure 34 and Figure 35, while the octet-cell sample results are in Figure 36, Figure 37, Figure 38, Figure 39 and Figure 40.

Figure 32 illustrates the stress-strain curve obtained on the cross-truss 4 mm length x 1 mm diameter lattice sample. By applying compression on the lattice, elastic deformation is started. By increasing the applied force, a shear band initiates and a sequence of struts along the main diagonal of the sample deforms plastically. After this stage, the thickness of the 'shear band' increases and the stress remains roughly constant.

Figure 33 illustrates the stress-strain curve obtained on the cross-truss 8 mm length x 2 mm diameter lattice sample. By applying compression on the lattice, elastic deformation is started, until suddenly rupture of the struts. This lattice exhibits a very brittle behavior.

Figure 34 illustrates the stress-strain curve obtained on the cross-truss 10 mm length x 1 mm diameter lattice sample. By applying compression on the lattice, elastic deformation is started. As this sample is much weaker, considerable noise is recorded during the experiment. The bottom part of the sample fails first, followed by one of the upper corners.

Figure 35 illustrates the stress-strain curve obtained on the cross-truss 20 mm length x 2 mm diameter lattice sample. By applying compression on the lattice, elastic deformation is started. This is followed by abrupt rupture of truss members in the middle of the sample, which results in immediate catastrophic failure.

Figure 36 illustrates the stress-strain curve obtained on the octet-truss 4 mm length x 1 mm diameter lattice sample. This sample deforms similarly to the cross-truss sample with the same strut dimensions (Figure 32). After an initial stage of elastic deformation, the

sample deforms plastically and a stress plateau is maintained up to very large strains. In this case, though, no shear band is observed.

Figure 37 illustrates the stress-strain curve obtained on the octet-truss 8 mm length x 2 mm diameter lattice sample. By applying compression on the lattice, elastic deformation is started, followed by plastic deformation and suddenly rupture of the struts. The lattice has a very brittle behavior, very similar to that of the cross-truss sample with struts of the same dimension (Figure 33).

Figure 38 illustrates the stress-strain curve obtained on the octet-truss 10 mm length x 1 mm diameter lattice sample. By applying compression on the lattice, elastic deformation is started, until suddenly rupture of struts and failure of the structure.

Figure 39 shows the sample after testing. In this case, crack propagations happened due to manufacturing imperfections on the structure. The cracks propagated between layers of the material.

Figure 40 illustrates the stress-strain curve obtained on the octet-truss 20 mm length x 2 mm diameter lattice sample. By applying compression on the lattice, elastic deformation is started until some vertical struts start to buckle, mainly on the boundaries of the sample. A shear band initiates and plastic deformation occurs on the struts that connect the boundaries of the shear band region. Meanwhile, other struts also buckle during the compression.

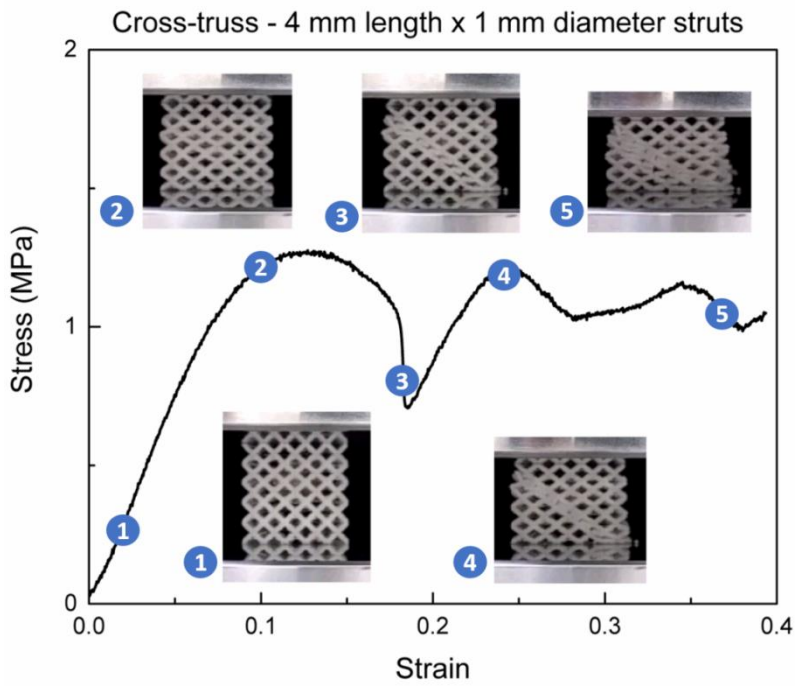

Figure 32: Experimental stress-strain curve of the cross-truss 4 mm length x 1 mm diameter lattice sample.

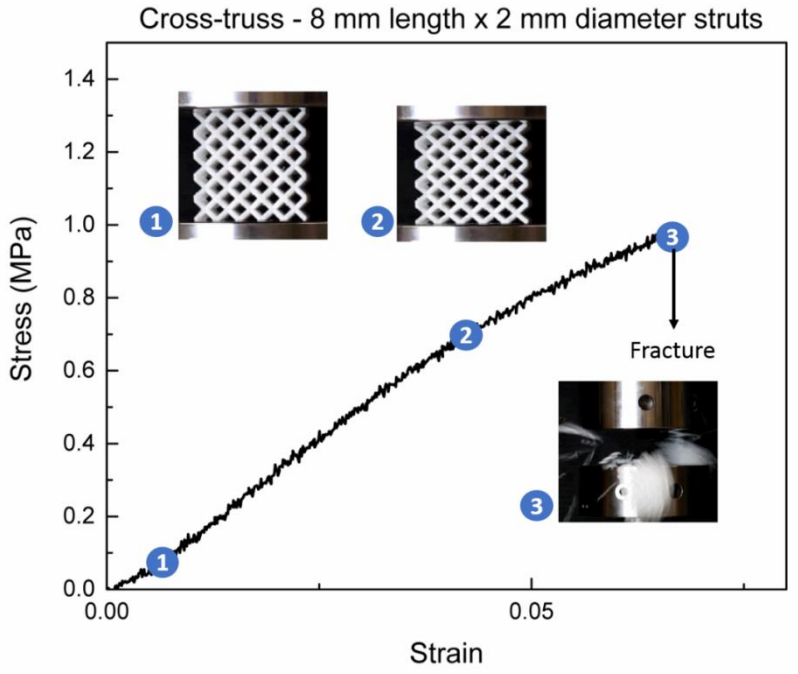

Figure 33: Experimental stress-strain curve of the cross-truss 8 mm length x 2 mm diameter lattice sample.

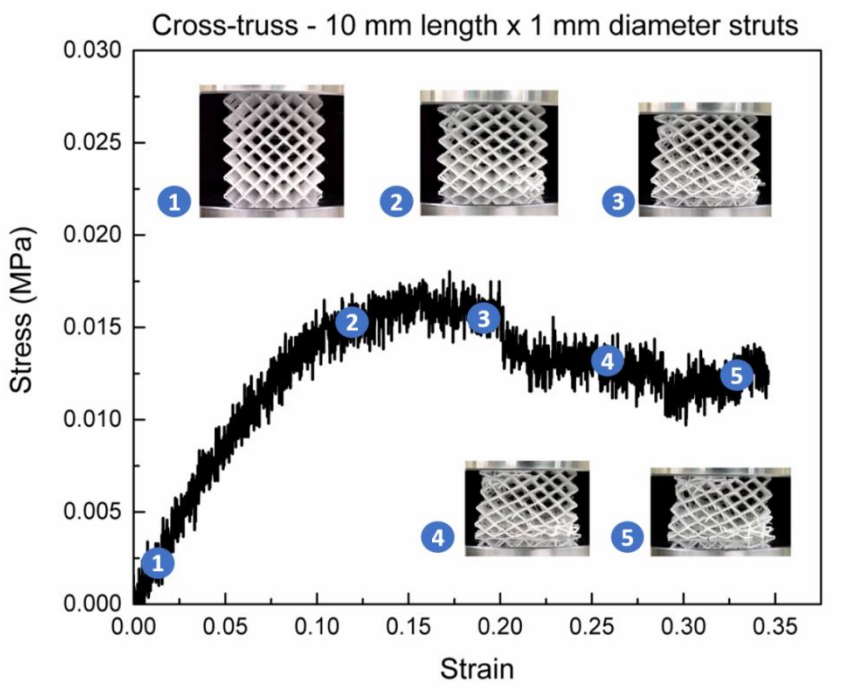

Figure 34: Experimental stress-strain curve of the cross-truss 10 mm length x 1 mm diameter lattice sample.

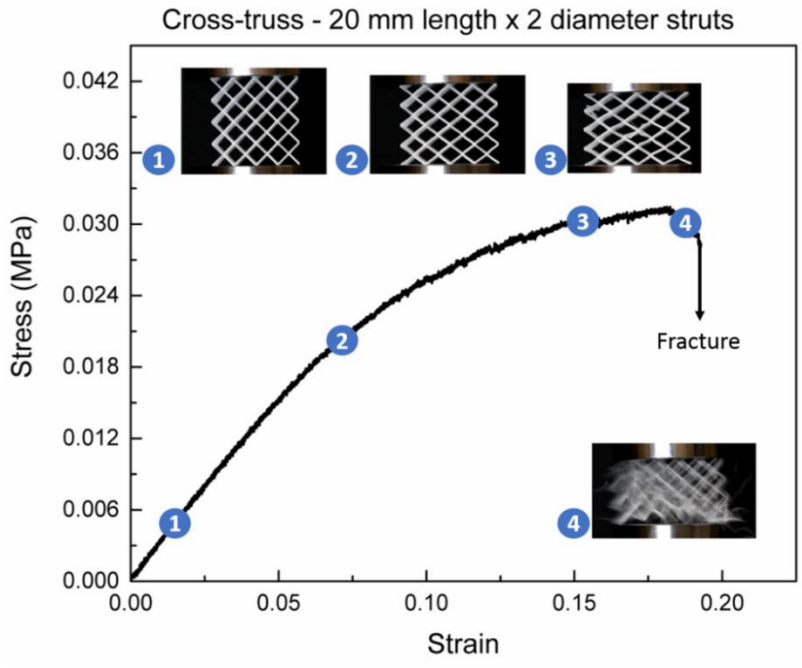

Figure 35: Experimental stress-strain curve of the cross-truss 20 mm length x 2 mm diameter lattice sample.

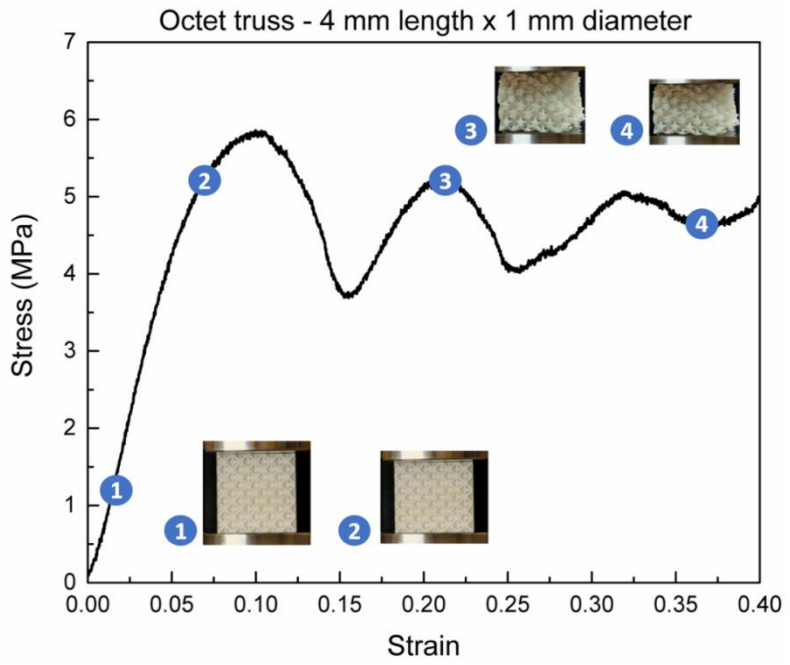

Figure 36: Experimental stress-strain curve of the octet-truss 4 mm length x 1 mm diameter lattice sample.

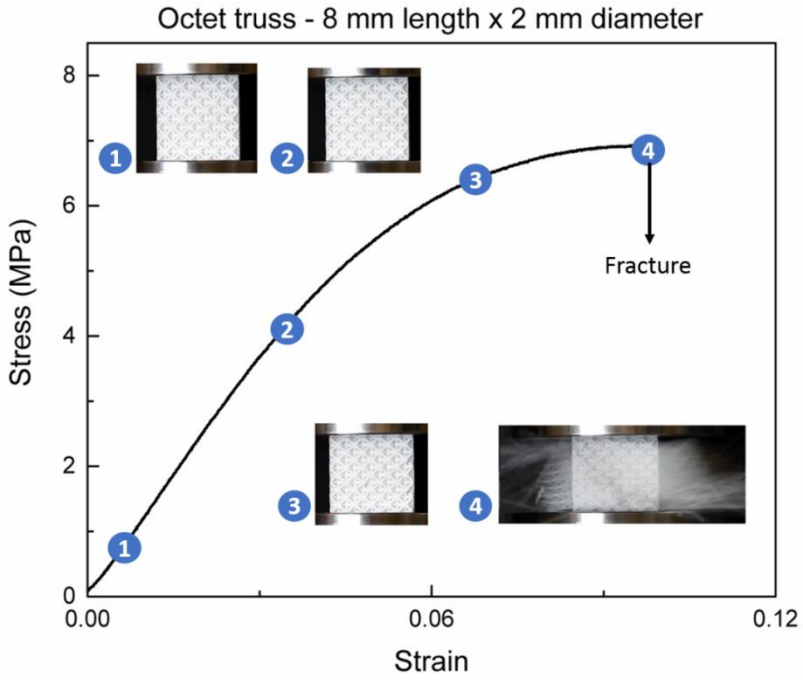

Figure 37: Experimental stress-strain curve of the octet-truss 8 mm length x 2 mm diameter lattice sample.

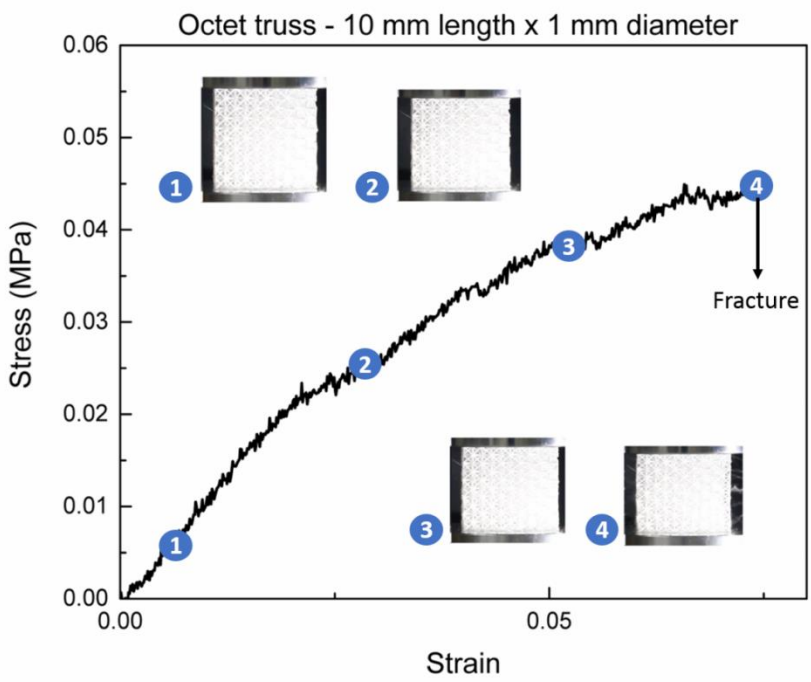

Figure 38: Experimental stress-strain curve of the octet-truss 10 mm length x 1 mm diameter lattice sample.

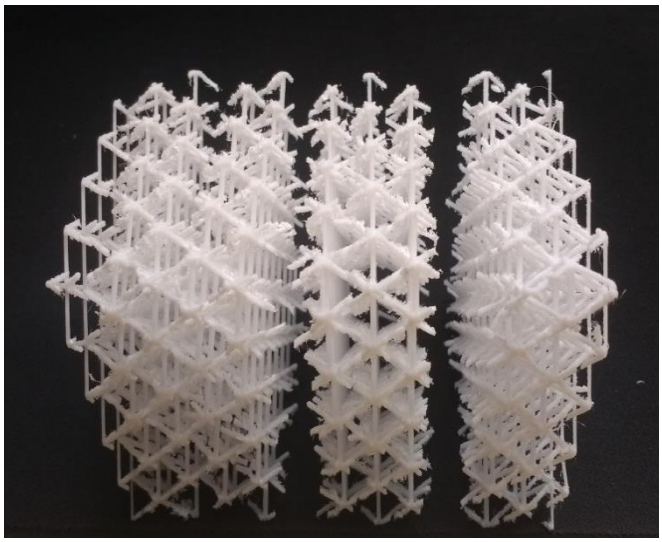

Figure 39: Octet-truss 10 mm length x 1 mm diameter sample after compression test.

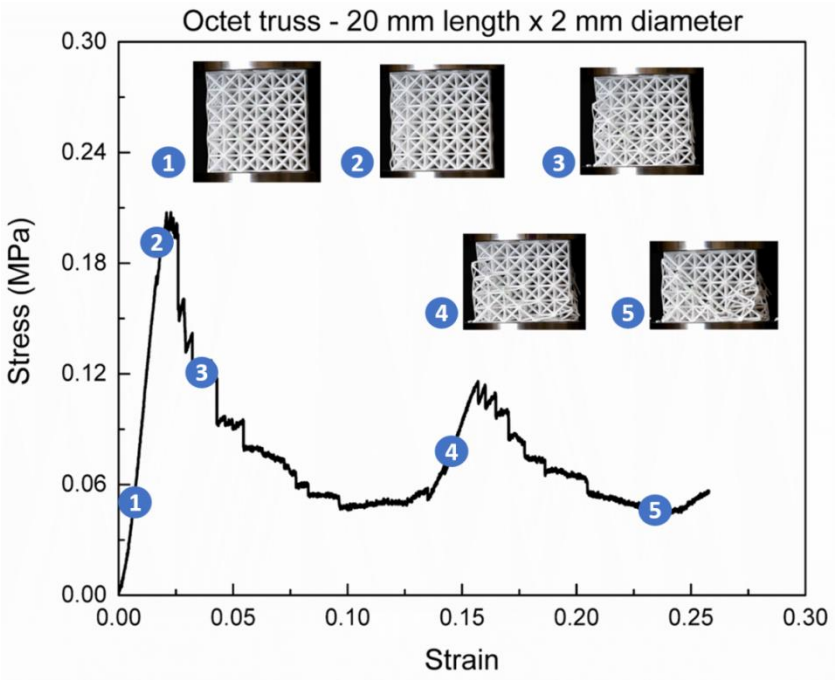

Figure 40: Experimental stress-strain curve of the octet-truss 20 mm length x 2 mm diameter lattice sample.

6. DISCUSSION

This chapter discusses and interprets the results obtained in this study.

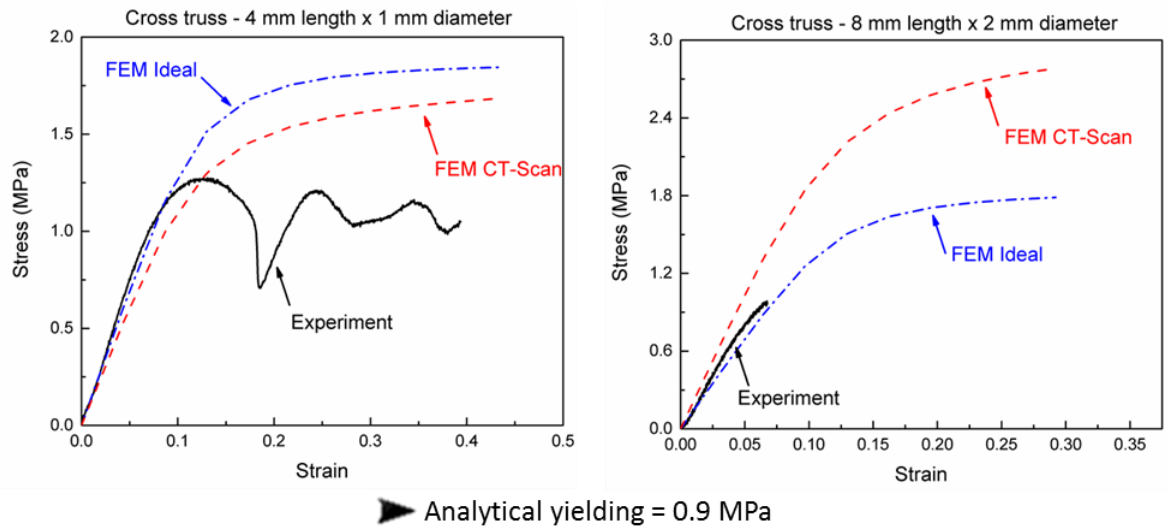

Figure 41: Stress-strain curves of experiment and simulations of the cross-truss 4 mm length x 1 mm diameter lattice (left) and 8 mm length x 2 diameter lattice (right).

Figure 41 shows the stress-strain curves of the uniaxial compression tests and simulations of the cross-truss samples made by struts with aspect ratio of 4 (stubby samples). A few key observations can be made: (i) the numerical models capture the stiffness of the samples quite well; (ii) although the analytical model and FEM simulation on the ideal unit cells are identical for the samples of different dimensions, the FE simulations on the CT-scanned geometries predicts a much higher strength for the 2mm diameter strut samples. This difference correlates well with a difference in relative density between the two samples: while for the cross-truss 4 mm x 1 mm unit cell the ratio between the density of the CT-Scanned cell and the ideal cell is 0.94, the same ratio is 1.2 for the 8mm x 2 mm cross truss unit cell; (iii) for the 4 mm x 1 mm sample, the yield strength is captured fairly well by the numerical simulations (as well as the analytical

model), although the FE simulations overpredict the plateau strength; (iv) the 8 mm x 2 mm sample failed in brittle fashion at a stress level lower than predicted by FE models, but consistent with analytical predictions for strut yielding. Given that the constituent material in the numerical models is characterized as elastic perfectly plastic with no damage model included, the simulations will not be able to capture fracture.

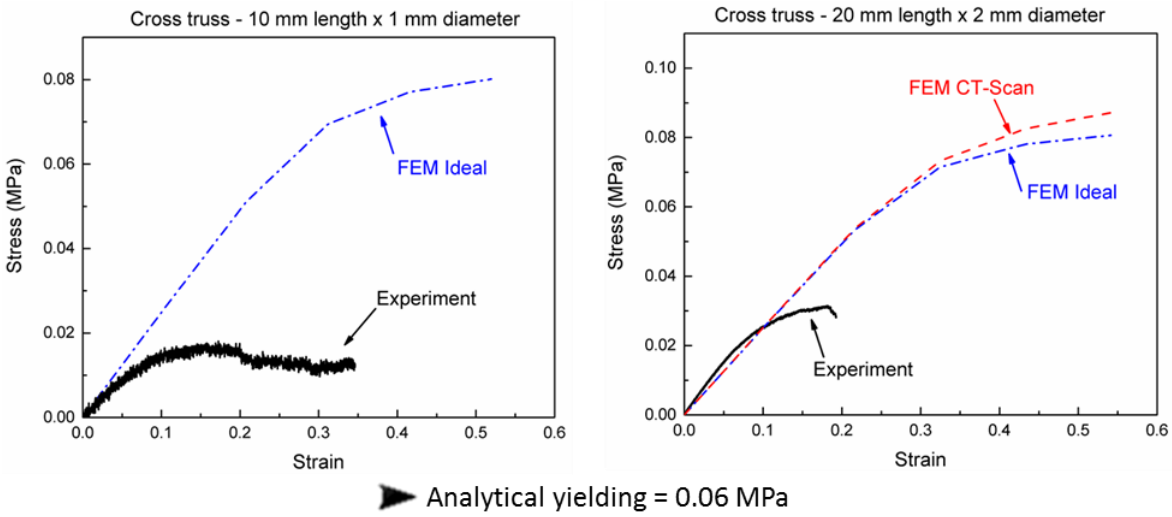

Figure 42: Stress-strain curves of experiment and simulations of the cross-truss 10 mm length x 1 mm diameter lattice (left) and 20 mm length x 2 diameter lattice (right).

Figure 42 shows the stress-strain curves of the uniaxial compression tests and simulations of the cross-truss samples made by struts with aspect ratio of 10. Notice that for both strut sizes, the FE simulations agree well with analytical predictions. The CT scanned (only available for the 2 mm diameter strut sample) and ideal geometries are nearly indistinguishable, indicating that the fabrication defects captured by CT scanning have negligible effect on the mechanical properties of the lattices. Importantly, though, all models significantly overpredict the strength of the samples. For the sample with the thinnest bars, this is largely attributed to a significant numbers of missing struts, as a result

of the support material removal step in the fabrication process. For the 2 mm diameter strut sample the lower strength is attributed to the fact that the sample is constituted by less unit cells than the previous ones, weakening the boundary conditions.

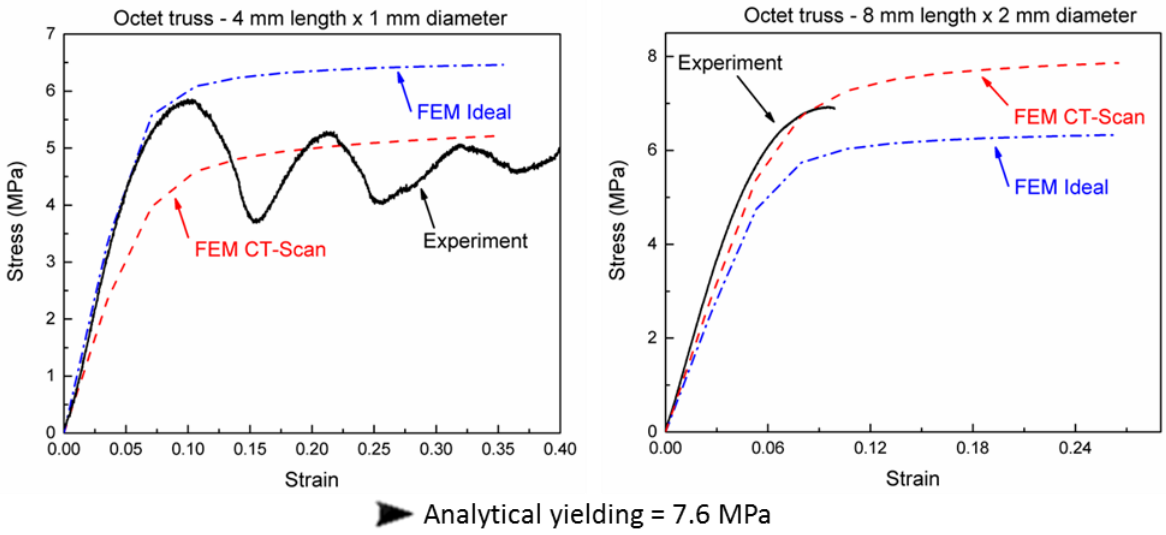

Figure 43: Stress-strain curves of experiment and simulations of the octet-truss 4 mm length x 1 mm diameter lattice (left) and 8 mm length x 2 diameter lattice (right).

Figure 43 shows the stress-strain curves of the uniaxial compression tests and simulations of the octet-truss samples made by struts with aspect ratio of 4 (stubby samples). Again, fracture of the specimens during experimental tests is not captured on the numerical simulations because of the definition of the material on the model as elastic perfectly plastic. The difference in strength between the FEM Ideal and CT-Scanned models is again related to the difference in density between ideal and fabricated model. While for the octet-truss 4 mm x 1 mm unit cell the ratio between the density of the CT-Scanned cell and the ideal cell is 0.81, the same ratio is 1.05 for the 8 mm x 2 mm octet truss unit cell. The increase of amount of material especially around the nodes substantially increases the strength of the unit cell. Notice that for both size samples, the numerical models are in good

agreement with the experiments. Interestingly, the 1mm-strut diameter sample is stronger than predicted by the CT-scanned model and in near-perfect agreement with the FE model on the ideal lattice; conversely, the 2mm- strut diameter sample performs as predicted by FE modeling on the CT-scanned sample.

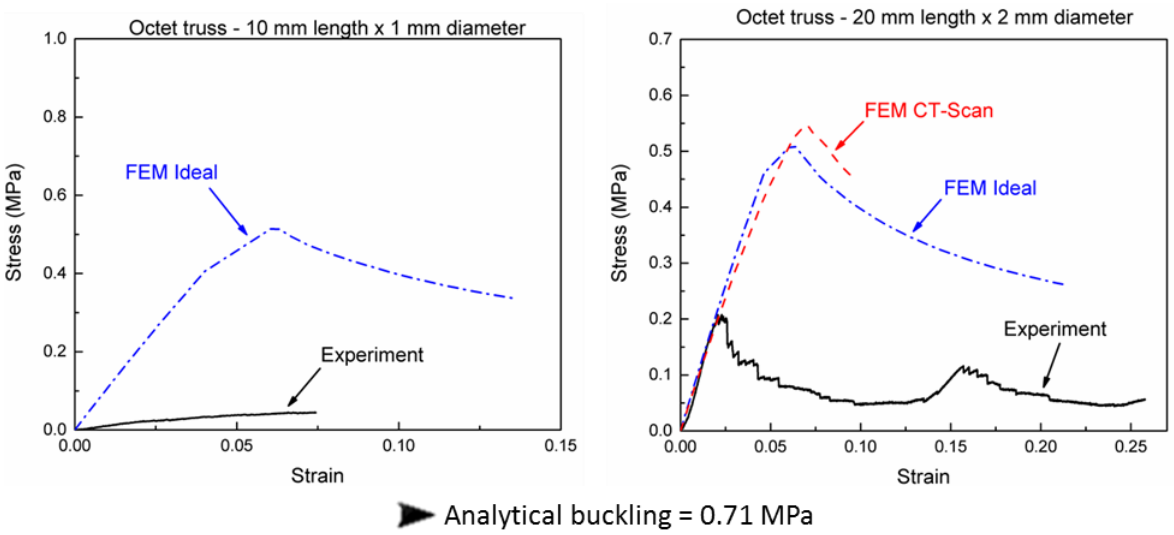

Figure 44: Stress-strain curves of experiment and simulations of the octet-truss 10 mm length x 1 mm diameter lattice (left) and 20 mm length x 2 diameter lattice (right).

Figure 44 shows the stress-strain curves of the uniaxial compression tests and simulations of the octet-truss samples made by struts with aspect ratio of 10 (slender samples). As analytical models predicted that these samples would fail by elastic buckling (at much lower load than required to yield the lattice), imperfections were seeded in the mesh for FE calculations. For the larger strut diameter lattice, the CT-scanned geometry sample showed nearly the same strength as the ideal geometry sample, according to FE calculations, indicating that the imperfections revealed by CT analysis do not have a dramatic effect on strength. No comparison is available for the 1mm strut diameter lattice, as that sample could not be scanned. The most remarkable result, though, is that the

samples are much weaker than predicted by both analytical and numerical models. This is largely attributed to significant imperfections in these lattices that were not captured by CT scanning, namely missing bars.

For the sample with 1 mm diameter struts, failure occurred by crack propagation on planes between layers, causing collapse of the structure at much lower stresses than predicted. For the sample with 2 mm diameter struts, failure occurred by buckling as predicted, albeit at a much lower critical stress. Buckling happened first on the bars located on the boundaries of the sample. When these bars fractured, it was observed that this fracture occurred between layers, leading to conclude that manufacturing imperfections were responsible for the lower strength.

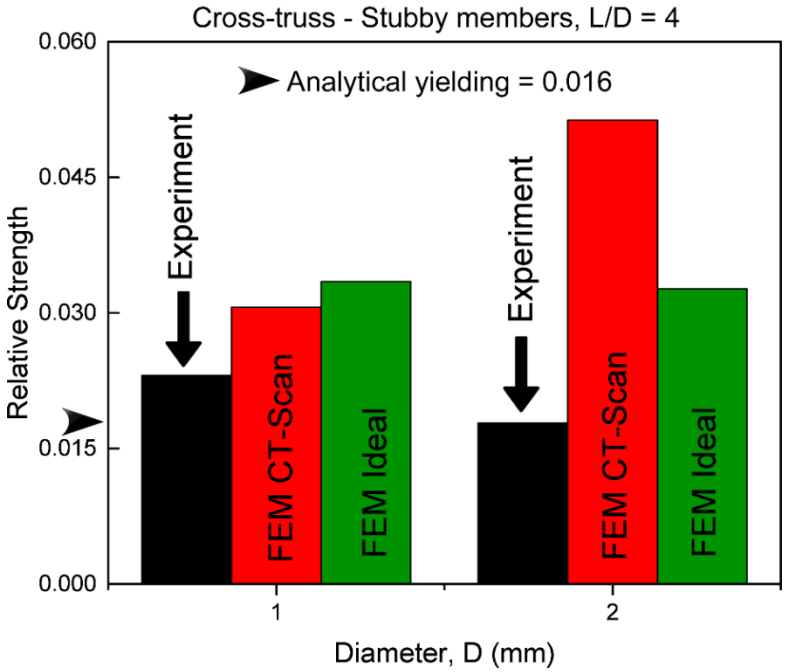

Figure 45: Summary of the relative strength of the cross-truss unit cell with aspect ratio = 4 obtained via analytical calculation, experiment and numerical modeling.

Figure 45, Figure 46, Figure 47 and Figure 48 summarize the strength of all structures studied in this work. The histograms are grouped according to the topology of the unit cell and aspect ratio of the struts. The ultimate strength, and not the onset of yielding or buckling, was chosen to be represented on these comparisons.

Figure 45 illustrates the relative strength of the cross-truss unit cells with aspect ratio of 4 obtained via analytical calculation, experiment and numerical models. The FEM results showed a higher strength because the ultimate strength was considered, and FEM ideal models were free of imperfections. The analytical model agrees well with the experiment results.

Figure 46 illustrates the relative strength of the cross-truss unit cells with aspect ratio of 10 obtained via analytical calculation, experiment and numerical models. Here the experiments showed a much lower strength than predicted by analytical model and FEM simulations. As explained above, this is largely attributed to manufacturing imperfections that were not captured by CT scanning of single unit cells, in particular missing bars.

Figure 47 illustrates the relative strength of the octet-truss unit cells with aspect ratio of 4 obtained via analytical calculation, experiment and numerical models. The experiments show good agreement with the models. The analytical model is slightly non-conservative for these samples.

Finally, Figure 48 illustrates the relative strength of the octet-truss unit cells with aspect ratio of 10 obtained via analytical calculation, experiment and numerical models. The experiments show a much lower strength than predicted by the analytical and numerical models. As explained in detail before, this is again due to the manufacturing imperfections that could not be captured by single unit cell CT scans, namely missing bars.

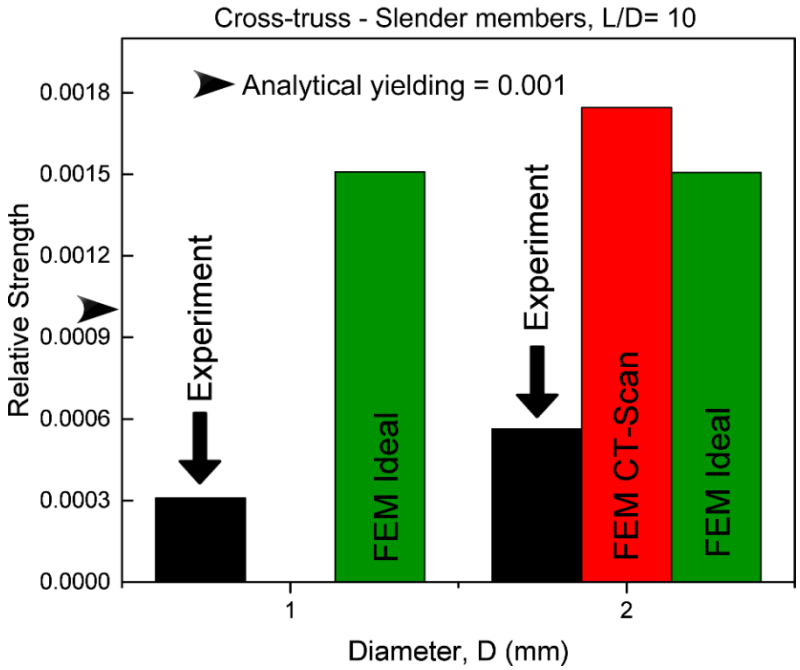

Figure 46: Summary of the relative strength of the cross-truss unit cell with aspect ratio = 10 obtained via analytical calculation, experiment and numerical modeling.

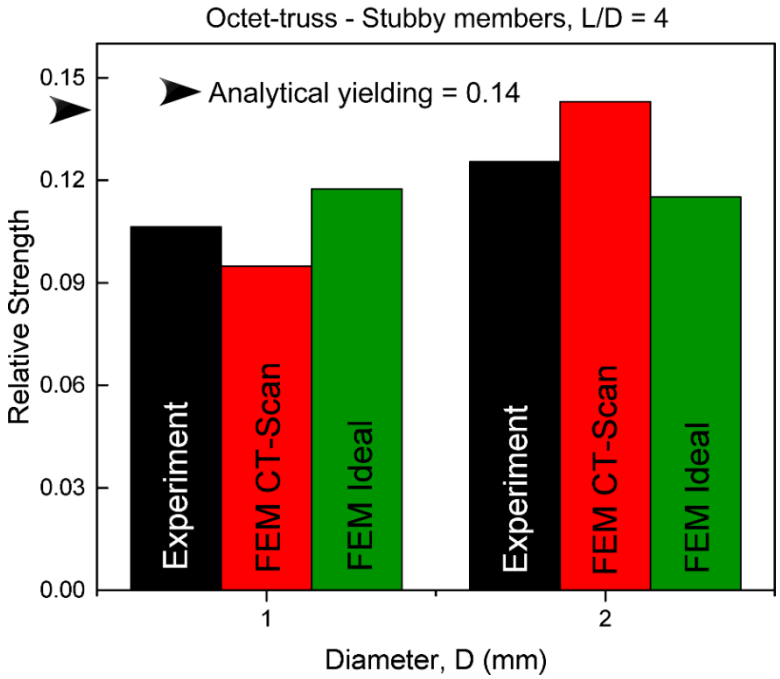

Figure 47: Summary of the relative strength of the octet-truss unit cell with aspect ratio = 4 obtained via analytical calculation, experiment and numerical modeling.

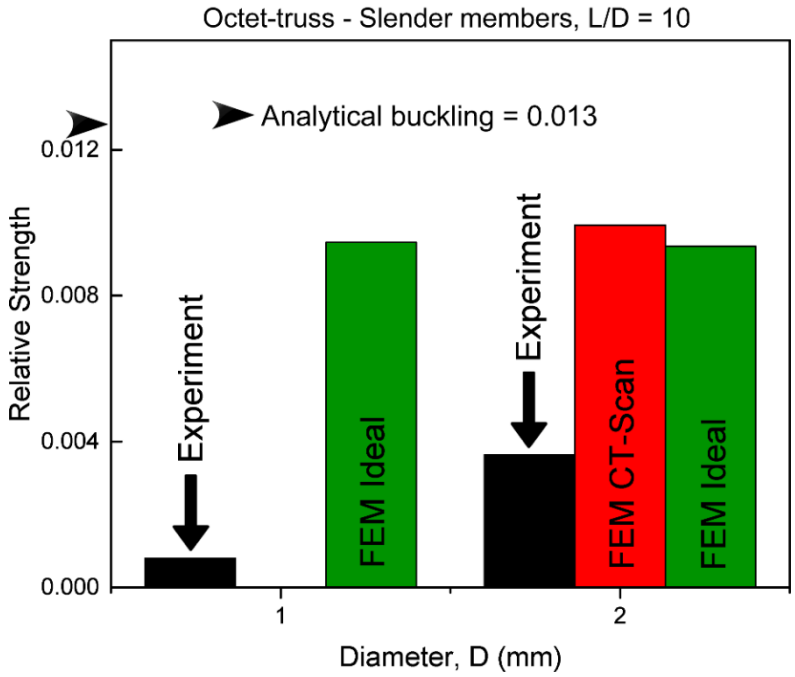

Figure 48: Summary of the relative strength of the octet-truss unit cell with aspect ratio = 10 obtained via analytical calculation, experiment and numerical modeling.

7. CONCLUSIONS

The present work aimed to study the effect of manufacturing defects on compressive strength of polymeric lattices fabricated via fused deposition modeling. To achieve this goal, unit cells were designed by varying topology (cross-truss and octet-truss), aspect ratio (4 and 10) and strut diameter (1 mm and 2 mm). All samples were manufactured using polycarbonate, due to good mechanical properties and market penetration. The material was experimentally characterized to understand the influence of layer deposition on the fabrication of parts.

After the fabrication, the samples were scanned with the goal of detecting imperfections and later enable the construction of finite element models. Imperfections were found both on the surface of the bars and in their interior. The compression experiments show that the samples with lower diameter and aspect ratio (4 mm x 1 mm) exhibit a strength plateau after reaching the compressive strength. The other samples displayed a more brittle behavior, disintegrating soon after reaching the compressive strength. CT scanning reveals that the manufactured lower aspect ratio samples (both cross and octet unit cell) are significantly denser than designed, clearly affecting their strength. The octet-truss samples with aspect ratio of 10, predicted to fail by elastic buckling, fail catastrophically at much lower loads than predicted by models, due to manufacturing imperfections.

The disagreement between analytical, FE models and experiments is due to imperfections caused by the manufacturing process, such as voids, variations on the diameter of the bars and density. This disagreement increases as the diameter of the struts decreases and aspect ratio increases.

8. BIBLIOGRAPHY

[1] Muthu, S. S., Savalani, M. M. (2016). Handbook of Sustainability in Additive Manufacturing, V.2. Springer, Singapore.

[2] [Online]. Available: http://study.com/academy/lesson/pneumatic-bones-in-birds.html.

[3] Meyers, M. A., Chen, P.-Y., Lin, A. Y., Seki, Y. (2008). Biological materials: Structure and mechanical properties. *Progress in Materials Science*, *53*(1), 1–206.

[4] Aremu, A. O., Maskery, I. A., Tuck, C. J., Ashcroft, I. A., Wildman, R. D., Hague, R. J. M. (2016). Effects of net and solid skins on self-supporting lattice structures. In *Conference Proceedings of the Society for Experimental Mechanics Series* (Vol. 2, pp. 83–89).

[5] Yan, C., Hao, L., Hussein, A., Raymont, D. (2012). Evaluations of cellular lattice structures manufactured using selective laser melting. *International Journal of Machine Tools and Manufacture*, *62*, 32–38.

[6] Lakes, R. (1993). Materials with structural hierarchy. *Nature*, *361*(6412), 511–515.

[7] Schaedler, T. A., Carter, W. B. (2016). Architected Cellular Materials. *Annual Review of Materials Research*, *46*(1), 187–210.

[8] Wieding, J., Wolf, A., Bader, R. (2014). Numerical optimization of open-porous bone scaffold structures to match the elastic properties of human cortical bone. *Journal of the Mechanical Behavior of Biomedical Materials*, *37*, 56–68.

[9] Thompson, M. K., Moroni, G., Vaneker, T., Fadel, G., Campbell, R. I., Gibson, I., Martina, F. (2016). Design for Additive Manufacturing: Trends, opportunities, considerations, and constraints. *CIRP Annals - Manufacturing Technology*, *65*(2), 737–760.

[10] Gibson, L. J., Ashby, M. F. (1997). Cellular Solids: Structure and Properties, 2nd ed. Cambridge University Press, Cambridge.

[11] Meza, L. R., Zelhofer, A. J., Clarke, N., Mateos, A. J., Kochmann, D. M., & Greer, J. R. (2015). Resilient 3D hierarchical architected metamaterials. *Proceedings of the National Academy of Sciences*, *112*(37), 11502–11507.

[12] Zheng, X., Lee, H., Weisgraber, T. H., Shusteff, M., DeOtte, J., Duoss, E. B., Spadaccini, C. M. (2014). Ultralight, ultrastiff mechanical metamaterials. *Science*, *344*(6190), 1373–1377.

[13] Wadley, H. N. (2006). Multifunctional periodic cellular metals. *Philosophical Transactions of the Royal Society A: Mathematical, Physical and Engineering Sciences*, *364*(1838), 31–68.

[14] Lu, T. J., Valdevit, L., Evans, A. G. (2005). Active cooling by metallic sandwich structures with periodic cores. *Progress in Materials Science*.

[15] Haghpanah, B., Salari-Sharif, L., Pourrajab, P., Hopkins, J., Valdevit, L. (2016). Multistable Shape-Reconfigurable Architected Materials. *Advanced Materials*, *28*(36), 7915–7920.

[16] Fratzl, P., Weinkamer, R. (2007). Nature's hierarchical materials. *Progress in Materials Science*.

[17] Maiti, A., Small, W., Lewicki, J. P., Weisgraber, T. H., Duoss, E. B., Chinn, S. C., Wilson, T. S. (2016). 3D printed cellular solid outperforms traditional stochastic foam in long-term mechanical response. Scientific Reports, 6(1), 24871.

[18] Wadley, H. N. G. (2002). Cellular metals manufacturing. *Advanced Engineering Materials*, *4*(10), 726–733.

[19] Vaidya, U., Nelson, S., Sinn, B., Mathew, B. (2001). Processing and high strain rate impact response of multi-functional sandwich composites. *Composite Structures*, *52*(3-4), 429–440.

[20] Smith, L., Wang, Y. S., Morrison, R., Smith, C. (2011). Aircraft floor and interior panels using edge coated honeycomb. *US Patent 7,988,809*, 1-20.

[21] Fleck, N. A., Deshpande, V. S., Ashby, M. F. (2010). Micro-architectured materials: past, present and future. *Proceedings of the Royal Society A: Mathematical, Physical and Engineering Sciences*, *466*(2121), 2495–2516.

[22] Schaedler, T. A., Jacobsen, A. J., Torrents, A., Sorensen, A. E., Lian, J., Greer, J. R., Carter, W. B. (2011). Ultralight Metallic Microlattices. *Science*, *334*(6058), 962–965.

[23] Asadpoure, A., Valdevit, L. (2015). Topology optimization of lightweight periodic lattices under simultaneous compressive and shear stiffness constraints. *International Journal of Solids and Structures*, *60*, 1–16.

[24] Deshpande, V. S., Ashby, M. F., Fleck, N. A. (2001). Foam topology: Bending versus stretching dominated architectures. *Acta Materialia*, *49*(6), 1035–1040.

[25] Ashby, M. F. et al. (2000). Metal Foams: A Design Guide, 1st ed. Butterworth-Heinemann, Oxford.

[26] Evans, A. G., Hutchinson, J. W., Fleck, N. A., Ashby, M. F., Wadley, H. N. G. (2001). The topological design of multifunctional cellular metals. *Progress in Materials Science*, 46(3–4), 309–327.

[27] Ashby, M. F. (2006). The properties of foams and lattices. *Philosophical Transactions. Series A, Mathematical, Physical, and Engineering Sciences*, *364*(1838), 15–30.

[28] ASTM (2010). F2792-10e1 Standard terminology for additive manufacturing technologies. ASTM International.

[29] Hull, C. W. (1986). Apparatus for production of three-dimensional objects by stereolithography. *US Patent 4,575,330*, 1–16.

[30] [Online]. Available: http://printinthemix.com/Fastfacts/Show/914.

[31] Huang, S. H., Liu, P., Mokasdar, A., Hou, L. (2013). Additive manufacturing and its societal impact: A literature review. *International Journal of Advanced Manufacturing Technology*.

[32] Masood, S. H. (2014). Advances in Fused Deposition Modeling. In *Comprehensive Materials Processing* (Vol. 10, pp. 69–91).

[33] Smith, W. C., Dean, R. W. (2013). Structural characteristics of fused deposition modeling polycarbonate material. *Polymer Testing*, *32*(8), 1306–1312.

[34] Ford, M. (2015). FDM Technology. *Stratasys Technology*, 1–24. Retrieved from http://www.stratasys.com/3d-printers/technologies/fdm-technology.

[35] [Online]. Available: http://blog.stratasys.com/2012/02/27/tips-for-quick-thorough-soluble-support-removal/.

[36] Ahn, D., Kweon, J. H., Kwon, S., Song, J., Lee, S. (2009). Representation of surface roughness in fused deposition modeling. *Journal of Materials Processing Technology*, *209*(15-16), 5593–5600.

[37] [Online]. Available: http://www.solidworks.com/

[38] Valdevit, L., Godfrey, S. W., Schaedler, T. A., Jacobsen, A. J., Carter, W. B. (2013). Compressive strength of hollow microlattices: Experimental characterization, modeling, and optimal design. *Journal of Materials Research*, *28*(17), 2461–2473.

[39] Salari-Sharif, L., Schaedler, T. A., Valdevit, L. (2014). Energy dissipation mechanisms in hollow metallic microlattices. *Journal of Materials Research*, *29*(16), 1755–1770.

[40] Dong, L., Deshpande, V., Wadley, H. (2015). Mechanical response of Ti-6Al-4V octet-truss lattice structures. *International Journal of Solids and Structures*, *60*, 107–124.

[41] Deshpande, V. S., Fleck, N. A., Ashby, M. F. (2001). Effective properties of the octet-truss lattice material. *Journal of the Mechanics and Physics of Solids*, *49*(8), 1747–1769.

[42] Dong, L., Wadley, H. (2016). Shear response of carbon fiber composite octet-truss lattice structures. *Composites Part A: Applied Science and Manufacturing*, *81*, 182–192.

[43] Elsayed, M. S. A., Pasini, D. (2010). Multiscale structural design of columns made of regular octet-truss lattice material. *International Journal of Solids and Structures*, *47*(14-15), 1764–1774.

[44] O'Masta, M. R., Dong, L., St-Pierre, L., Wadley, H. N. G., Deshpande, V. S. (2017). The fracture toughness of octet-truss lattices. *Journal of the Mechanics and Physics of Solids*, *98*, 271–289.

[45] Fan, H. L., Jin, F. N., Fang, D. N. (2009). Nonlinear mechanical properties of lattice truss materials. *Materials and Design*, *30*(3), 511–517.

[46] [Online]. Available: http://www.stratasys.com/.

[47] [Online]. Available: http://www.smg3d.co.uk/3d_design_software/insight_software.

[48] Karamooz Ravari, M. R., Kadkhodaei, M., Badrossamay, M., Rezaei, R. (2014). Numerical investigation on mechanical properties of cellular lattice structures fabricated by fused deposition modeling. *International Journal of Mechanical Sciences*, *88*, 154–161.

[49] [Online]. Available: http://www.xradia.com/versaxrm-410/.

[50] [Online]. Available: https://www.simpleware.com/.

[51] Hibbeler, R. C. (2011). Mechanics of Materials. Pearson Prentice Hall (Vol. 8).

[52] [Online]. Available: https://www.3ds.com/products-services/simulia/products/abaqus/.

[53] [Online]. Available: http://www.instron.us/en-us/products/testing-systems/dynamic-and-fatigue-systems/8860-electric-actuator.